Review

Graphene-Based Derivatives Heterostructured Catalytic Systems for Sustainable Hydrogen Energy via Overall Water Splitting

Iqra Sadiq, Syed Asim Ali and Tokeer Ahmad *

Nanochemistry Laboratory, Department of Chemistry, Jamia Millia Islamia, New Delhi 110025, India
* Correspondence: tahmad3@jmi.ac.in; Tel.: +91-11-2698-1717 (ext. 3261)

Abstract: The global climate crisis has cultivated the demand for sustainable energy resources as fossil derivative fuels are functional in catalyzing the rate of environmental breakdown. Sustainable energy solutions generate various renewable energy prospects capable of delivering efficient energy operations. Among these prospects, green H_2 energy generated via overall water splitting is an effective approach towards sustainability ascribed to the higher gravimetric density and efficiency of H_2 fuel. In this review, we sought to discuss the applicability and challenges of graphene-based derivatives in H_2 evolution operations through photochemical, electrochemical and photoelectrochemical water-splitting pathways. The unique layered structure of graphene-based derivatives alongside marvelous optoelectronic and physicochemical properties ease out the thermodynamic uphill of water splitting better than their non-layered counterparts. In addition, the heterojunction formation in the graphene derivatives with visible light catalysts propels the kinetics of HER. Functionalized GO and rGO derivatives of graphene are riveting catalysts that have received extensive interest from researchers attributed to their accelerated chemical and mechanical stability, tunable band structure and larger surface area, providing more exposed active sites for HER. The surface organic functional groups of GO/rGO assist in establishing synergetic interfacial contact with other catalysts. Thus, these groups provide structural and chemical versatility to GO/rGO-based heterostructured catalysts, which effectively improve their physicochemical parameters that drive their catalytic performance towards HER. In order to develop a cost-effective and highly efficient catalytic system, graphene-based derivatives are promising heterostructured catalysts that exhibit a good relationship between catalytic efficiency and robustness.

Keywords: sustainable energy; graphene; hydrogen energy; overall water splitting; heterojunctions

1. Introduction

The world is running headlong towards a dearth of energy as the limited supply of fossil fuel sources and their derivatives fail to adequately meet current operational demand. The spike in the energy prices of conventional energy resources in recent years has triggered the researchers to look beyond them as the energy crisis has far-reaching consequences, which are not limited to just energy scarcity but rather propelling several environmental catastrophes as well. In a broader sense, the price rise in energy inflicts the price rise of finished goods as the cost of manufacturing escalates; thus, the economy destabilizes due to inflation, as recently experienced by the once-flourishing nation of Venezuela. Correspondingly, the offshoots of fossil fuel usage are not so environmentally friendly, and the pollution caused by fossil fuels is calamitous. It is a well-known fact that air pollution is an invisible killer. Recent research has reported that 8.7 million premature deaths were globally accounted for in 2018 due to the burning of fossil fuels, which caused a substantial exposure of PM 2.5 [1–3]. It was found in a study that the air pollution caused by fossil fuels is culpable for nearly one out of every five deaths worldwide [4]. At

present, more than 80% of the global energy requirement is fulfilled by fossil fuel sources and their derivative fuels [5]. These circumstances are navigating the world to immediate concerns and indicate an important potential lesson for future energy strategies. Another catastrophic situation of the COVID-19 pandemic has put the world at a crossroads, as oil demand faced a historic decline worldwide at the time of the shutdown, which has rebounded again in 2021 and, as expected, demand will increase in the coming years, as depicted in Figure 1a [6].

Despite the impact of COVID-19, in 2021, energy demand increased by 4.6%, more than counterpoising the 4% shrinkage in 2020 [7]. According to the United States Energy Information Administration (USEIA), global energy demand will rise to 47% by 2050. At this critical point, the world can switch to replenishable energy sources that are environmentally benign. Renewable energy is the best possible alternative to fossil fuels as it is more sustainable than its fossil counterparts [8,9]. Hydrothermal, geothermal, wind and solar energies are renowned renewable energy reservoirs that are clean, abundant and trustworthy for reducing pollution and the impact of global warming [10]. Renewable energy solutions (RESs) are the focal point of the energy transition to subdue carbon emissions due to their more sustainable nature [11,12]. RESs have expanded rapidly in recent decades, and there has been steady growth in their scalability and applicability. The brightest spot of RESs remains the electricity sector; nevertheless, electricity only accounts for one-fifth of global energy consumption. The role of renewable energy in the heating and transportation sectors is still a question that needs to be answered, as shown in Figure 1b [13]. To accomplish cost-effectiveness and high reliability, more comprehensive, flexible energy systems and complex policy measures are required. In recent decades, hydrogen (H_2) extracted through green pathways has been appreciated as a remedy for resolving multiple environmental issues because it is the epitome of clean fuel [14–16]. When green H_2 energy is used as a fuel, it not only attributes as an excellent efficiency in energy transformation but also emerges as a zero-pollution producer as it yields water as a by-product, which does not require further treatment [17–21]. H_2 has emerged as a promising alternative to fossil fuels. Hydrogen is the most common and abundant element in the universe, even though it never exists by itself [22,23]. Hydrogen always occurs in a combined form with other elements, such as carbon and oxygen [24]. Nevertheless, once separated, it is an excellent carrier of clean energy [25]. The use of H_2 as an alternative fuel is not a new topic to discuss, as it has played an essential role in global energy systems in recent decades. However, till now, its scope of applicability has been very specific and limited. A fruitful changeover to a H_2 economy would bring immense benefits, including the reduction and sequestration of carbon emissions from the decreased use of hydrocarbons, the mitigation of fossil fuels depletion and would also be helpful in meeting the energy needs of the increasing population [26–35]. According to International Energy Agency (IEA) data, the demand for H_2 and its derivative products has increased by 300% since 1975 in various applications. Figure 1c illustrates the global demand for pure H_2 from 1975 to 2018 [36]. Additionally, in the coming decades, the IEA estimates a continued increase in H_2 use and expects a 30% increase in global hydrogen use in the transportation sector by 2070. It also reckons the growth in H_2 employment for the production of ammonia and synthetic kerosene by 10% and 20%, respectively, in the coming decades. Figure 1d depicts the IEA estimation of the global demand for H_2 by different sectors under a sustainable development scenario for the coming five decades [37]. There are a number of conventional methods for H_2 production, such as the electrolysis of water and sodium borohydride through hydrolysis or pyrolysis. Sodium borohydride ($NaBH_4$) hydrolysis to produce hydrogen can occur under ambient conditions [38]. $NaBH_4$ can be prepared by utilizing different methods and can achieve high yields. The $NaBH_4$ solution from hydrolysis reactions releases a 90% stoichiometric amount of H_2. The $NaBH_4$ solubility in water is comparatively low; therefore, the hydrolysis needs more water than required by stoichiometry to make certain the solubility of $NaBH_4$ [39]. Though, $NaBH_4$ can be treated as a water-splitting agent because 50% of the hydrogen produced is from water. Another traditional method is water electrolysis, where water splits into oxygen

and hydrogen via the utilization of electrical energy. Generally, the electrolysis of water system consists of a cathode, an anode segregated by an electrolyte and a power supply. The electrolyte is commonly made up of an aqueous solution that contains ions and an oxygen ion-exchange membrane or a proton-exchange membrane. Water electrolysis is not a spontaneous process due to the negative standard global potential. Thus, it needs a power source (an external intervention), and the reaction can be written as H_2O + electricity $\rightarrow H_2 + 1/2\, O_2$ [40].

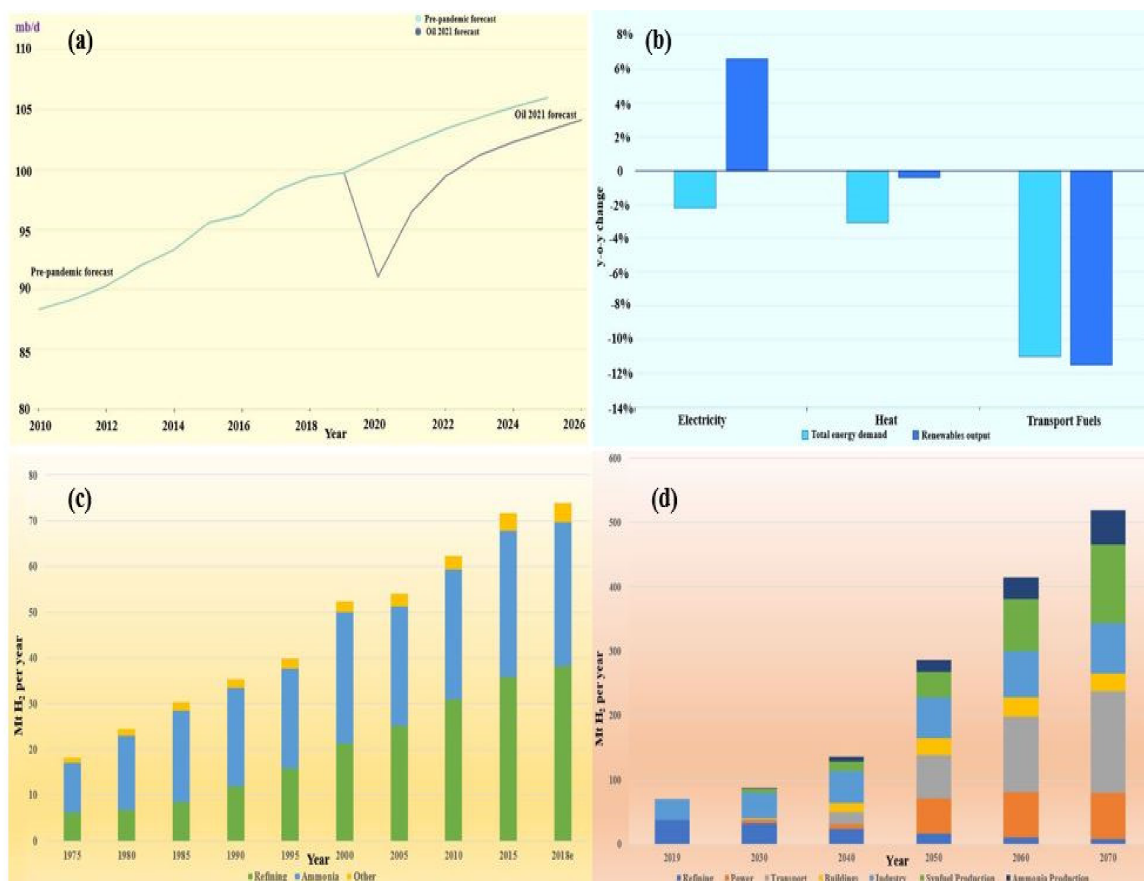**Figure 1.** (**a**) Oil demand forecast, 2010–2026, pre-pandemic and in Oil 2021 [6]. (**b**) Change in energy demand and renewables output in electricity, heat and transport, 2019 to 2020 [13]. (**c**) Global demand for pure hydrogen, 1975–2018 [36]. (**d**) Global hydrogen demand by sector in the Sustainable Development Scenario, 2019–2070 [37].

One of the most economical and efficient ways of H_2 production is overall water splitting (OWS) [41]. OWS is a chemical approach that enables H_2 evolution by breaking the water into its elemental composition, hydrogen and oxygen [42]. The transformation of solar light energy into chemical energy using a photocatalytic system is known as photochemical water splitting (PWS), which can generate H_2 and O_2 [43,44]. In 1972, PWS operation for H_2 generation was the novel work of Fujishima and Honda, who used TiO_2 as the photocatalyst [45]. The most plentiful, clean, natural and renewable energy resources on Earth are water and sunlight [46]. Their transformation to H_2 has been reported to be an ideal solution to reduce fossil fuel use and the environmental problems related to fossil fuels [47]. The PWS process is considered to be the most efficient and renewable option for H_2 generation [47–50]. In this process, reductive and oxidative reactions take place simultaneously under solar light illumination [51]. H_2 can also be generated from OWS by utilizing the electricity produced by renewable energy sources, which is known as electrochemical water splitting (EWS) [52]. The rate of simultaneous half-reactions of water splitting taking place, hydrogen evolution reaction (HER) and oxygen evolution reaction

(OER) depend on the overpotential values of an efficient electrocatalytic system [53,54]. The production of H_2 through EWS has become a remarkable strategy for transforming electrical energy to clean H_2 fuel [55]. In recent years, thanks to the global interest in solar energy research, photoelectrochemical (PEC) water splitting has received significant attention. PEC imitates the natural photosynthesis Z-scheme, which is where photogenerated electrons (or holes) transfer to a cathode (or anode) surface to participate in the H_2 reduction (or oxidation) reaction. As the reaction sites are segregated spatially in this route, H_2 and O_2 do not need to be sequestered by external means. More so than any other pathway, H_2 generation through PEC proved cost-effective in the scenario of depleted fossil fuels [56]. Presently, we are dealing with such metals that are not at all cost-effective in nature, for example, Pt, Pd, Rh and Au, which are noble metal catalysts. They possess great potential to confront both energy and environmental problems, although they are very expensive and inefficient to work with. Expensive metal catalysts are affected by their shortage and comparatively low stability, which hinder their general use in large-scale applications. Consequently, catalysts with higher activity and lower cost are imperatively needed for large-scale practical applications [57]. Table 1 includes the advantages and disadvantages of the photochemical, electrochemical and photoelectrochemical methods.

Table 1. Advantages and disadvantages of photochemical, electrochemical and photoelectrochemical methods.

Methods	Advantages	Disadvantages
Photochemical	Uses most abundant sources (solar energy and water), economically and environmentally benign.	Limited properties of photocatalysts, requires doping or cocatalysts for enhanced photocatalytic conversion efficiency.
Electrochemical	Eco-friendly, sustainable energy	Expensive as the most effective electrocatalysts are Pt, Ru, etc.
Photoelectrochemical	Comprises electrical and photon energy, more efficient than photochemical and electrochemical pathways	More expensive than photochemical and electrochemical pathways

Lately, graphene-based catalytic systems have earned tremendous attention from the research community to bring about sustainable operations. In 2010, K.S. Novoselov and A.K. Geim were honored with a Nobel Prize for their innovative experiments on graphene. This provided an enormous boost to the present research and utilization of graphene and similar materials in an interdisciplinary field of sciences [58]. Graphene possesses a unique sp^2 bonded carbon monolayer, accelerated electrical and thermal conductivity (nearly about 5000 W m^{-1} K^{-1}), a very high theoretical surface area (~2600 m^2/g), mechanical strength and excellent charge carrier mobility at room temperature (2×10^5 cm^2 V^{-1} s^{-1}) [59,60]. All of these properties mean that graphene and graphene-based materials are promising candidates for applications that enable producing environmentally friendly green H_2 energy, as demonstrated in Figure 2. Due to the fact that the fabrication sketch of graphene and its derivatives does not vary drastically, we have not gone into detail with its synthetic literature [61]. However, the synthesis of graphene and its derivative-based heterostructures has made steady progress, and various diverse modern synthetic approaches have been developed to design graphene and its derivative-based catalytic systems with diverse nanostructures [62,63]. The usual trait among all of the chemical routes is not only to escalate the ultimate physiochemical properties but also to generate a greater number of catalytically active sites [64,65]. Thus, in order to have the required morphology and surface-area-driven nanocatalysts, it is essential to utilize innovative synthetic routes, such as hydrothermal/solvothermal methods [66,67], chemical vapor deposition (CVD) [68], the reverse-micellar method [69,70] and polymeric citrate precursor (PCP) route [71,72].

Figure 2. Diagrammatic representation of multi-functional properties of graphene.

El-Maghrabi et al. [73] synthesized a $NiTiO_3$/graphene photocatalyst that exhibited a higher H_2 evolution rate compared to bare $NiTiO_3$ nanoparticles. This can be ascribed to an effectual separation of photo-generated charged carriers, the strong absorption of light in the visible region and lowered charge carrier recombination. Du et al. [74] designed a Ru/Graphene catalyst, which exhibited exceptionally high catalytic activity for H_2 generation. This noteworthy refinement of catalytic activity is believed to be due to the synergistic effect of Ru nanoparticles with graphene. As a further matter, these examples may open up a new path for the preparation of other nanoparticles supported with graphene for enhancing H_2 generation.

Among the diverse classes of graphene, one is graphene oxide (GO), an oxidation product of graphene. Due to its low production cost, it is one of the most important graphene derivatives [75]. GO contains various oxygen functional groups (OFGs), namely hydroxyl, epoxy and carboxyl groups, due to which its plane becomes bulkier. GO is hydrophilic and water soluble in nature due to the presence of OFGs, and in aqueous solutions, it forms stable suspensions [76,77]. GO is easy to fabricate, and in many scientific fields, it is the preferred choice of material for discrete applications [78]. Furthermore, because of the presence of OFGs in GO, it has better chemical reactivity in comparison to graphene. GO has the upper hand over other carbon-based compounds, such as graphene, diamond, carbon nanotubes and fullerenes, because of its wide specific surface area and time–cost-effective synthesizing process. Wang et al. [79] prepared MoS_2/g-C_3N_4/GO as an effective photocatalyst for H_2 generation utilizing solar energy. GO with a high surface area performed as a very good conductive substrate for increasing the mobility of photo-charged carriers. As a result, the H_2 evolution rate and photocurrent density of MoS_2/g-C_3N_4/GO ternary composite improved significantly than the MoS_2/g-C_3N_4 photocatalyst. $CdS/ZnO/GO$ and CdS/Al_2O_3/GO were synthesized by Khan et al. [80] to examine the photochemical activity of these compounds. Both of the compounds showed an enhanced photocatalytic response, which was attributed to GO nanosheets, providing higher surface area for easy charge transfer and effective mass transfer that retarded the recombination frequency of photo-induced electron–hole pairs. These results highlight the specific characteristics of GO, which is an exceptional material for electron transporters and collectors to segregate the photo-generated charge carriers. Additionally, these studies open up new avenues for the production of highly effective GO-based heterostructured catalysts driven by visible light that can be utilized for H_2 generation via OWS.

Reduced graphene oxide (rGO) is another marvelous derivative of graphene, which can be synthesized by several methods, including thermal and chemical methods, so that the oxygen content can be minimized for enhanced stability [81]. The flowchart of the fabrication of graphene and its derivatives using different chemical and physical routes is

illustrated in Figure 3. GO, in its regular oxidation state, has subdued sensitivity making it electrically insulating due to the presence of OFGs. Although, reducing GO through thermal or chemical methods, such as hydrogen sulphide, dimethylhydrazine, aluminium powder, hydrazine hydrate vapor and $NaBH_4$, can regain the conductivity by reducing the oxygen content and maintaining the double bond of aromatic carbon atoms [82–88]. After processing using these methods, few OFGs remain in the GO. Despite that, it does not transform into graphene after thermal and chemical submission. As a result, rGO exhibits advanced stability and conductivity, making it a potential candidate for various applications in science [89]. Park et al. [90] synthesized $MoSe_2$-rGO heterostructures, which revealed exceptional HER response having diminished the Tafel slope and overpotential values attributed to the synergistic effect between $MoSe_2$ nanocrystals and rGO nanosheets and their specific porous structures. Cu_2ZnSnS_4 (CZTS)/MoS_2-rGO has been synthesized by Ha et al. [91]. The photochemical H_2 generation rate of CZTS was enhanced by 320% as MoS_2-rGO was incorporated. The photo-generated electrons of CZTS can be easily transferred to MoS_2 by using an rGO backbone, resisting the recombination of electron–hole pairs. These results are ascribed to the synergistic effect of the increased catalytically active sites of MoS_2 and the high charge separation tendency of rGO. To conclude, after considering these results, easy and cheap preparation methods for graphene and its derivatives are aspiring catalytic supports the building of an effective catalyst for H_2 generation. The multi-functional applications of graphene-based derivatives are schematically represented in Figure 4. Table 2 includes the preparation methods, most cost-effective routes and the properties of graphene, graphene oxide and reduced graphene oxide.
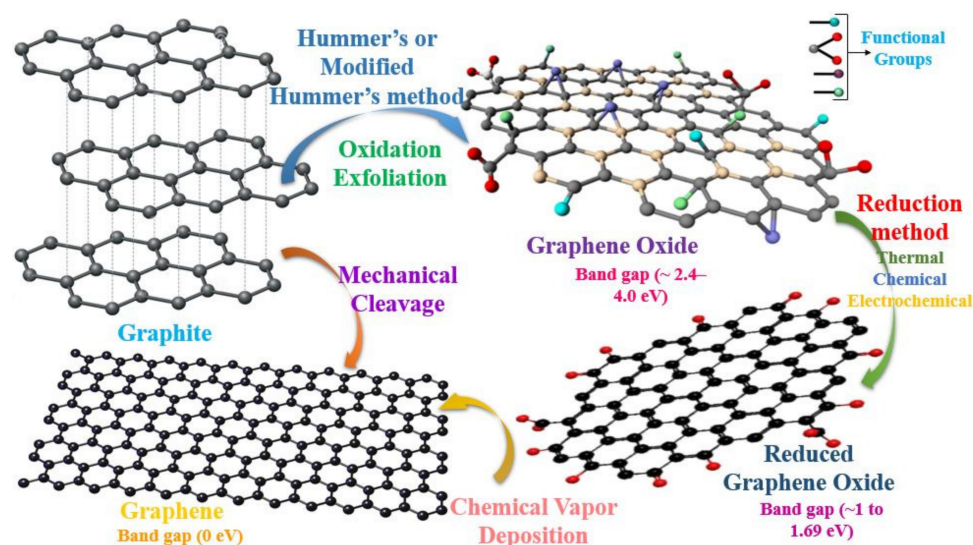

Figure 3. Flowchart of fabrication graphene and its derivatives through different chemical and physical routes.

Table 2. Preparation methods, cost-effective route and properties of graphene and its derivatives.

| Material	Preparation Methods		Cost-Effective Method		Properties
Graphene	Top-down method	Bottom-up Pyrolysis, Epitaxial Growth, Laser ablation CVD, Plasma Synthesis	Top-down	Bottom-up	Good electronic properties; High mechanical strength; High surface area; Tunable optical properties.
	Mechanical Exfoliation, Electrochemical, Chemical Exfoliation, Chemical Fabrication		Electrochemical	Laser ablation	
Graphene Oxide	Brodie Method, Staudenmaier Method, Hummers Method, Modified Hummers Method, Improved Hummers Method		Improved Hummers method		High colloidal constancy; Good dispersion in water; Contains rich oxygenated functional groups.
Reduced Graphene Oxide	Chemical exfoliation, Reduction methods (Thermal, Chemical, Electrochemical, Hydrothermal, Photochemical)		Chemical reduction		Greater electron transport properties; Restoration of sp^2 domains.
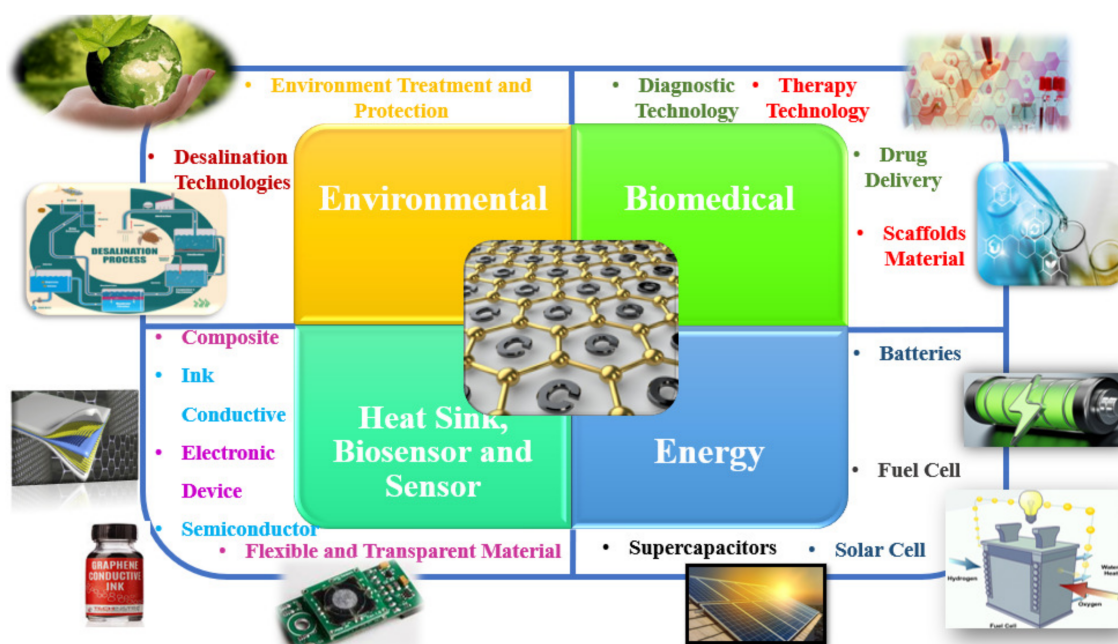
Figure 4. Multi-functional applications of graphene and its derivative based composites.

2. Scope of the Review

The thought process that motivated us to review the current successes of graphene-based derivatives for green H_2 energy solutions is their unique layered structure and advanced physiochemical properties. Graphene heterostructured catalytic systems have the caliber to replace noble-metal-based HER catalysts, which are inefficient due to their whopping cost. There are scattered reviews that discuss the catalytic efficiency of graphene and its derivatives; however, we aim to review their thorough applicability in photochemical, electrochemical and photoelectrochemical overall water splitting operations as these are exceptionally green routes that produce H_2 efficiently without generating toxic by-products. We have meticulously discussed the recent reports of graphene derivatives with critical insight into their HER performance.

3. Photocatalytic H_2 Production

Enhancing the photochemical response of photocatalysts is basically reliant on four factors that are (a) inhibiting the recombination of photo-induced electron–hole pairs, (b) tailoring the band gap of photocatalysts in the visible light region, (c) suitable catalytic support acting as a co-catalyst and (d) a higher specific surface area as it provides more adsorption sites [3,14,41,92]. To improve the photocatalytic activity, an efficient photocatalytic system should possess durable photo-induced charge carriers, fewer charge-capturing sites and a suitable band gap [93–96]. The mechanism of PWS for H_2 generation is displayed in Figure 5. Many efforts have been undertaken in recent decades to enhance the photocatalytic performance of catalysts, including modifications to the structure, tuning the bandgap and the interfacial heterostructuring of semiconductor photocatalysts [97–103]. In general, graphene and graphene-based derivatives act as catalytic supports with primary photocatalysts to improve their photochemical activity. Their tendency to accelerate the kinetics of photocatalytic reactions has recently received attention in the last decade [104–107].

Generally, pristine semiconductors show relatively inadequate photocatalytic activity because of the limited absorption of light energy and quick recombination of photo-excited electron–hole pairs [108]. These disadvantages can be effectively conquered by coupling graphene and its derivatives with appropriate photocatalytic materials, in particular metal chalcogenides, metal oxides and organic semiconductors [109,110]. Graphene and its derivatives containing one or two different photocatalytic materials are denoted as binary

and ternary graphene, GO- or rGO-based heterostructures. The main purpose for fabricating such types of binary and ternary heterostructures is to attain optimized photocatalysts that are able to utilize a wide spectrum of solar light, restrain the quick recombination rate of photo-excited charge carriers and possess excellent robustness and stability [111,112]. Such advantageous features of graphene and graphene derivative-based photocatalysts need to be advanced to compose next-generation cost-effective photocatalytic systems for the transformation of solar energy [113,114]. A schematic illustration of binary and ternary graphene and its derivatives-based heterostructures are depicted in Figure 6a,b, respectively, and Figure 6c illustrates the different photocatalysts with their corresponding band gaps.
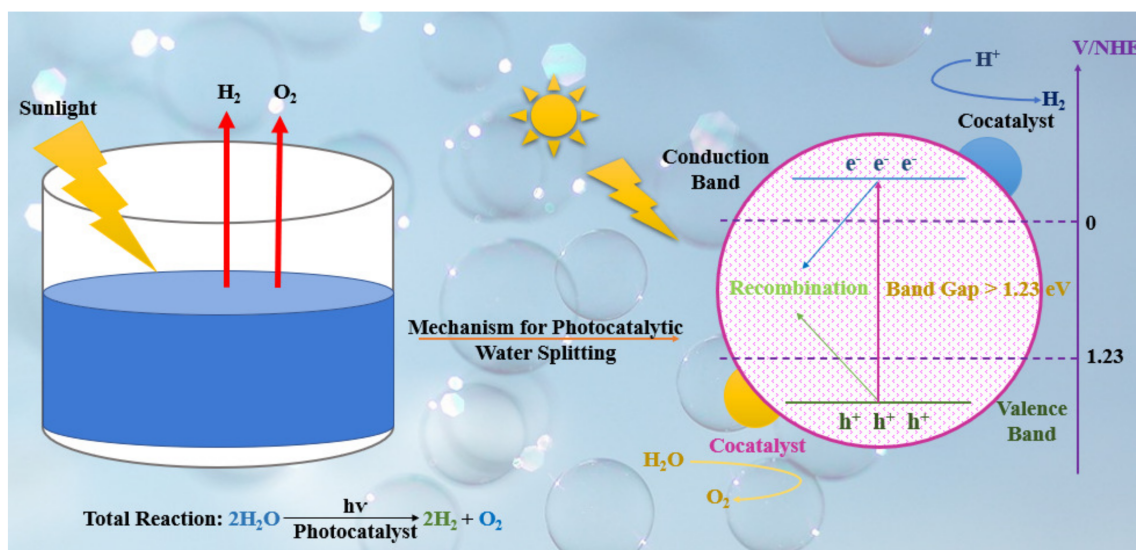

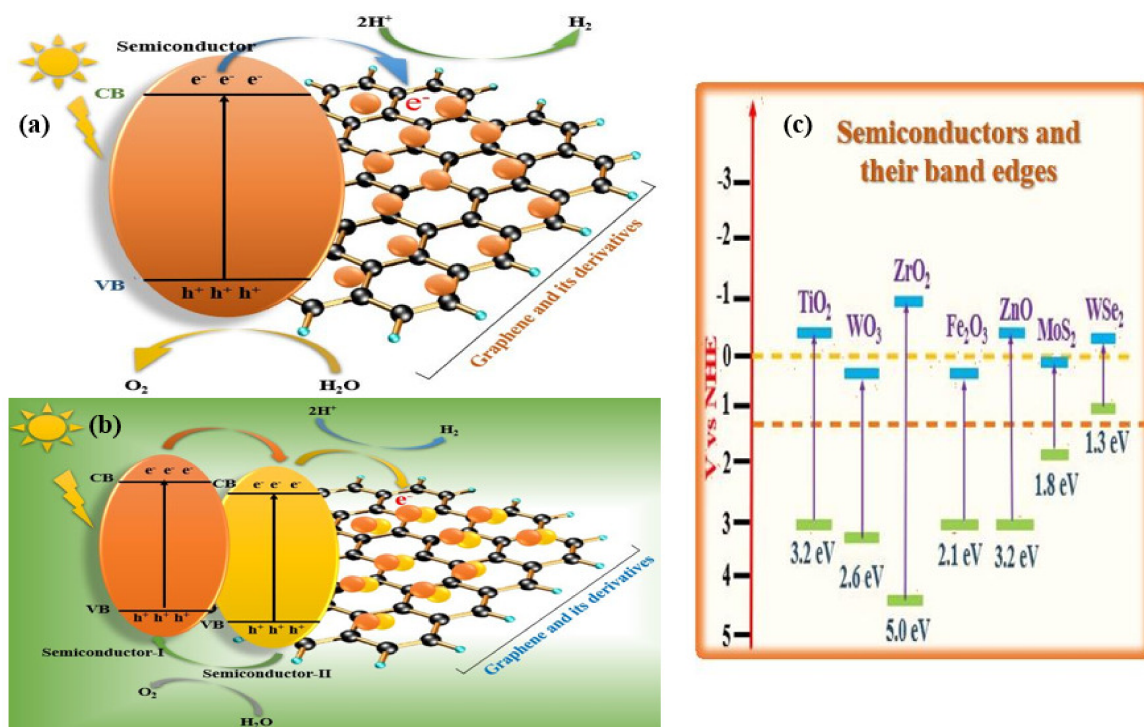**Figure 5.** Mechanism of photocatalytic water splitting for hydrogen generation.

Figure 6. (**a**) Photocatalytic sketch of binary graphene and its derivatives-based composite, (**b**) Photocatalytic sketch of ternary graphene and its derivatives-based composite and (**c**) Different semiconductors with their corresponding band gaps.

4. Graphene as a Photocatalyst

There have been numerous studies emphasizing the cogent design of graphene-based heterostructured photocatalysts with remarkable photocatalytic performance. Graphene is renowned for having a two-dimensional layered support that enhances the specific surface area of the photocatalytic system, and its circuit board exhibits an appealing potential, which leads to the effective utilization of the magnificent redox and electrical properties [115]. Khalid et al. [116] synthesized Ag-TiO$_2$/graphene photocatalysts to examine and compare their photochemical activity with respect to pristine TiO$_2$, TiO$_2$/graphene and Ag-TiO$_2$ samples. The results of the Ag-TiO$_2$/graphene showcased the noticeably improved H$_2$ generation activities compared to pristine TiO$_2$, TiO$_2$/graphene and Ag-TiO$_2$ samples. This improved photocatalytic H$_2$ generation performance was ascribed to the extended visible light absorption, the suppressed recombination of photo-induced electron–hole pairs and the increased surface area. This report exhibited the synergistic relationship of graphene incorporation into a metal oxide photocatalyst with UV band energy. However, a noble-metal-free photocatalyst could be employed for environmental friendliness. Xia et al. [117] fabricated CdS nanoparticles that were anchored on graphene nanoribbons (GNR). As-prepared CdS/GNR nanocomposites showed excellent photocatalytic activity for H$_2$ evolution, as the highest achieved H$_2$ evolution rate was 1.89 mmol h^{-1} g^{-1}. The ameliorated results were attributed to the enhanced charge segregation efficiency, extended carrier lifetime and expedited surface transport reactions of the photo-induced charge carriers. In a reported work, Yu et al. [118] engineered ternary CdS/MoS$_2$/graphene nano-heterostructures to examine the H$_2$ production rate through PWS. The as-prepared CdS/MoS$_2$/graphene composites exhibited as high as 1.9 mmol h^{-1} g^{-1} H$_2$ evolution rate, which can be attributed to the anchored graphene that acted as a charge transporter along with the electron acceptor for the exceptional performance of the CdS/MoS$_2$/graphene synergistic system. The charge recombination suppressed in CdS due to the graphene existence and the electron transfer of synergistic system played an important role in improving the photochemical activity for H$_2$ generation. Another ternary photocatalytic system, CdS/Nb$_2$O$_5$/N-doped graphene for H$_2$ generation, was synthesized by Yue et al. [119]. The results demonstrated a noteworthy photochemical performance for H$_2$ generation as the highest amount of H$_2$ evolved was 800 µmol g^{-1} under 8 h of visible light irradiation, which was 7.7-fold higher than that of pure CdS. The enhanced results were attributed to the escalated surface-area-to-volume ratio, enhanced photo-induced charge carrier separation and the outstanding electronic conductivity of N-doped graphene. Khalid et al. [120] prepared Eu-TiO$_2$/graphene composites to investigate their PWS performance. The superior properties of the as-developed composites, such as the inhibited recombination of electron–hole pairs and increased visible light absorption simultaneously, were due to the fact that the synergistic effect of Eu and graphene resulted in excellent photocatalytic activity for H$_2$ production. Ni-doped ZnS-graphene photocatalysts were prepared by Chang et al. [121] to investigate their photocatalytic activity for H$_2$ evolution. The as-synthesized graphene/Ni-doped ZnS nanocomposites showed effective results, as the highest photocatalytic performance for H$_2$ evolution achieved was 8683 µmol h^{-1}g^{-1}. The upgraded results were accredited to the synergistic effect between graphene and ZnS, which accelerated the transfer of photo-induced electrons, increased the surface area and also enhanced the dispersing properties. In a study, Xiang et al. [122] reported WS$_2$/Graphene-CdS(CWG) ternary heterostructured nanocatalysts for H$_2$ evolution via PWS, as demonstrated in Figure 7a. Due to the combined effect of WS$_2$ and graphene, the physicochemical properties of the ternary composites amended the reduction in charge recombination and improved the interfacial charge transfer, resulting in efficient photocatalytic performance. The H$_2$ evolution rate achieved from the as-prepared ternary composites CWG with a 4.2 molar ratio of WS$_2$ and graphene to CdS was the highest, which was 1842 µmol h^{-1}g^{-1}, as shown in Figure 7b.

Chang et al. [123] investigated and compared the photocatalytic activity of ZnO-ZnS/graphene photocatalysts with ZnO-ZnS, as shown in Figure 8a. The optimum rate of the H$_2$ evolution of ZnO-ZnS/graphene with a weight ratio of 0.05 reached 1070 µmol h^{-1}g^{-1},

which was 5.5 times that of ZnO-ZnS, as shown in Figure 8b. Graphene incorporation led to an increase in the separation rate of photo-generated charge carriers and decreased the interface resistance. Additionally, the exceptional photocatalytic activity of ZnO-ZnS/graphene was attributed to the extended light absorption and effective transfer of photo-induced electrons. The stability of the as-prepared photocatalysts was also tested using three repeated cycles, as depicted in Figure 8c. Raghavan et al. [124] synthesized Graphene QDs/TiO$_2$ nanocomposites for photocatalytic H$_2$ generation. The as-prepared photocatalysts exhibited excellent photocatalytic activity with a very high hydrogen generation rate of 29,548 μmol g^{-1} h^{-1}, which is almost 14 times higher than pure P25 TiO$_2$.
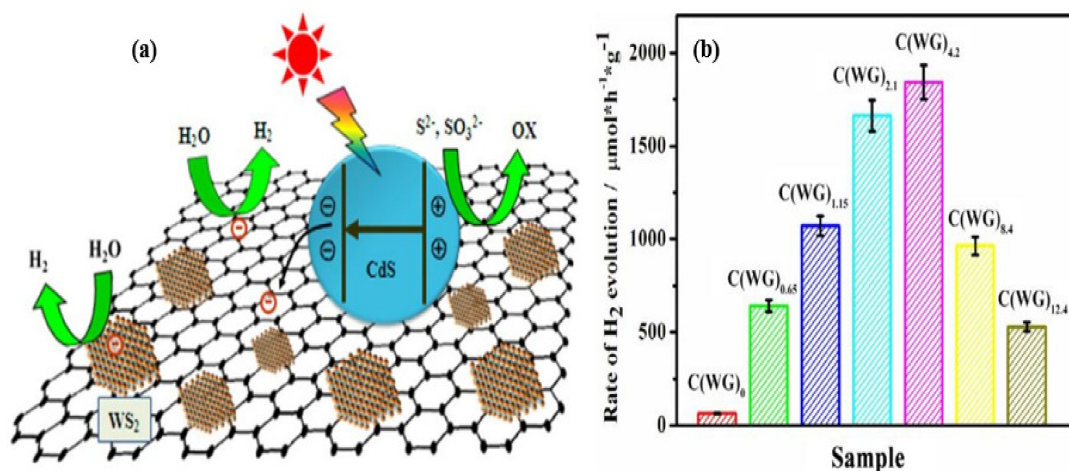

Figure 7. (**a**) Schematic illustration of the tentative mechanism proposed for the high H$_2$-production activity of the ternary CWG composite and (**b**) Comparison of the photocatalytic activity of the C(WG)$_0$, C(WG)$_{0.65}$, C(WG)$_{1.15}$, C(WG)$_{2.1}$, C(WG)$_{4.2}$, and C(WG)$_{12.4}$ samples for the photocatalytic H$_2$ production. (Reprinted with permission from reference [122]. Copyright 2016, John Wiley and Sons).
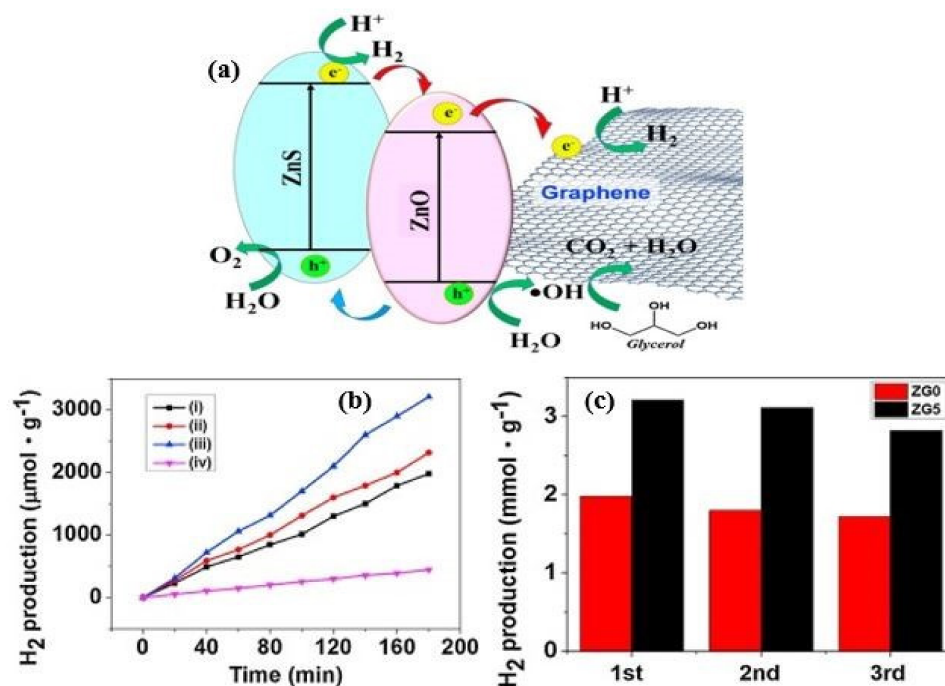

Figure 8. (**a**) Illustration of water-splitting reactions over the ZnO-ZnS/graphene photocatalyst under light irradiation. (**b**) The amount of produced H$_2$ by (i) ZG0, (ii) ZG1, (iii) ZG5 and (iv) ZG10 photocatalysts prepared at different graphene/ZnO-ZnS weight ratios during 3 h irradiation. (**c**) Photostability of recycled ZG0 and ZG5 photocatalysts with 3 h of irradiation for each test. (Reprinted with permission from reference [123]. Copyright 2018, Elsevier).

The aforementioned results of the graphene-based photocatalysts proved to be propitious photocatalytic materials for the future of H_2 generation through PWS. The presence of graphene in the above-mentioned heterostructures enhanced the photochemical H_2 generation rate of the photocatalysts by possessing an increased range of light absorption, higher specific surface area and outstanding electron conductivity.

5. Graphene Oxide as a Photocatalyst

Graphene oxide, with a diverse band gap between 2.4–4.3 eV and favorable chemical and physical features, proved to be an efficient photocatalyst for H_2 generation [125]. A wide number of studies have reported on the encouraging results of graphene oxide as a photocatalytic material for PWS. Gao et al. [126] engineered graphene oxide-CdS-Pt nanocomposites to examine H_2 generation through PWS. The optimum H_2 evolution rate observed was 123 mL $h^{-1}g^{-1}$, which was nearly 10-fold greater than pure CdS. This exceptional result was attributed to the synergistic effect of GO and Pt with CdS, in which GO played the role of an electron acceptor to resist the recombination of photo-induced charge carriers, enhancing photocatalytic activity. In another work, Rahman et al. [127] fabricated ternary GCN (graphitic carbon nitride)/ACN (amorphous carbon nitride)/GO heterostructures to investigate photocatalytic activity for H_2 generation. The results demonstrated an exceptional H_2 evolution rate of 251 μmol h^{-1}, which was ascribed to the synergistic effect that remarkably accelerated the segregation of photo-induced electron–hole pairs and subdued the recombination of charge carriers. The migration and collection of photo-induced electrons by GO expanded the reduction surface, which in turn enhanced the photocatalytic activity of the GCN/ACN/GO heterostructures. Sulfur-doped-graphene oxide quantum dots (S-GO QDs) were prepared and examined for photocatalytic H_2 generation by Gliniak et al. [128]. The H_2 evolution rate was obtained as 30.519 mmol $h^{-1}g^{-1}$ in 80% ethanol aqueous solution and in pure water as 18.166 mmol $h^{-1}g^{-1}$ with a prolonged lifespan of the photocatalyst. The nanocomposite GO-C_3N_4-LaVO$_4$ was prepared by Zhou et al. [129] to test the photocatalytic activity for H_2 generation, as shown in Figure 9a. The as-prepared GO-C_3N_4-LaVO$_4$ demonstrated stable and superior photocatalytic performance with a H_2 evolution rate of 717.6 μmol $g^{-1}h^{-1}$, as shown in Figure 9b. The effective results had significant benefits due to the enhanced charge separation and extended light absorption of the photocatalyst. The stability of the as-prepared photocatalyst proved remarkable even after long-term exposure to irradiation, as shown in Figure 9c.
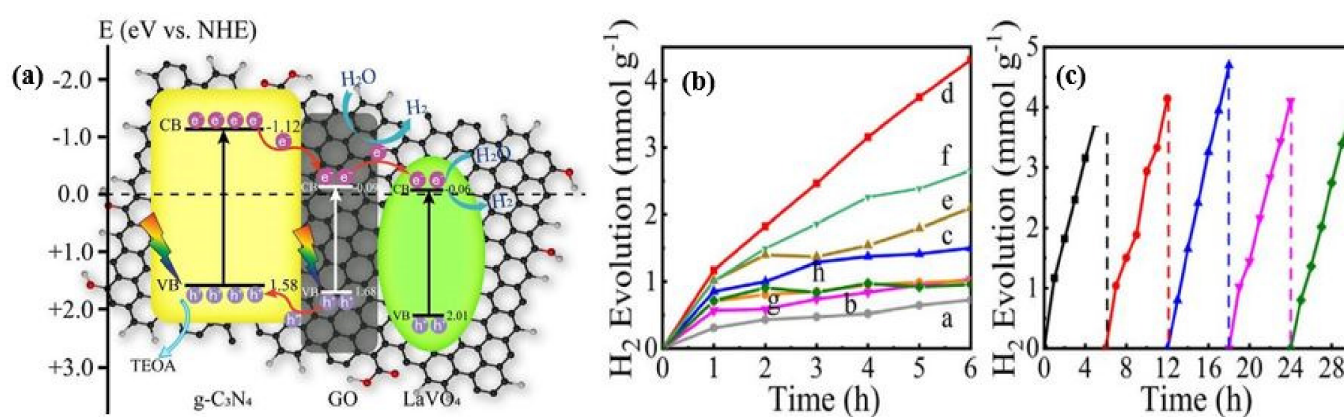

Figure 9. (**a**) Photo-produced electron transfer scheme over the GO-C_3N_4-LaVO$_4$ composite. (**b**) Dynamic curves of H_2 produced over the as-prepared GO-C_3N_4-a, the physical mixture of GO-C_3N_4 and LaVO$_4$-b, the physical mixture of GO, C_3N_4 and LaVO$_4$-c, GO-C_3N_4 (1:1)-LaVO$_4$ nanocomposite-d, g-C_3N_4-LaVO$_4$-e, GO-LaVO$_4$-f, pure g-C_3N_4, g- and LaVO$_4$-h, respectively. (**c**) Cyclings of H_2 production over the GO-C_3N_4-LaVO$_4$ composite. (Reprinted with permission from reference [129]. Copyright 2021, Elsevier).

In a reported work, Tie et al. [130] prepared a Pt/GO-ZnS photocatalyst that exhibited exceptional photocatalytic activity for H_2 production by yielding it at an evolution rate of 1082 $\mu mol\ h^{-1}g^{-1}$, which was far better than pure ZnS. The excellent performance of Pt/GO-ZnS was attributed to the synergistic effect of GO and Pt, which extended visible light harvesting and increased interfacial charge transfer. Pei et al. [131] designed a nitrogen-doped TiO_2/GO, which exhibited enhanced photocatalytic activity for H_2 generation with a 716 $\mu mol\ h^{-1}g^{-1}$ evolution rate under UV light irradiation. This could be ascribed to the narrowing of the band gap by GO and the synergistic effect of the fast electron transfer of photo-induced electrons and the effective electron capturing of GO resisting charge recombination. Gao et al. [132] prepared AgBr/polyoxometalate/graphene oxide (AgBr/POM/GO) ternary composites for H_2 evolution reactions under different reaction conditions where the POMs were PW_{12}, PMo_{12}, SiW_{12}, P_2Mo_{18} and P_2W_{18}. The utilization of AgBr/POM/GO was optimized, and the outcomes illustrated that the optimum amount of catalyst was 5 mg, as shown in Figure 10a; also, the optimization amount of AgBr in the as-prepared composites was 5%, as shown in Figure 10b. Further reaction conditions checked were the pH value adjustment and the sacrificial agent amount; the best sacrificial amount was found to be $TEOA/H_2O$ with 10% (V/V), as shown in Figure 10c, and the optimum pH value for the reaction was 7.5, as illustrated in Figure 10d. The as-fabricated $AgBr/PMo_{12}/GO$, $AgBr/PW_{12}/GO$, $AgBr/SiW_{12}/GO$, $AgBr/P_2Mo_{18}/GO$ and $AgBr/P_2W_{18}/GO$ heterostructures obtained average H_2 evolution rates of 256.0 $\mu mol\ g^{-1}\ h^{-1}$, 223.2 $\mu mol\ g^{-1}\ h^{-1}$, 212.0 $\mu mol\ g^{-1}\ h^{-1}$, 177.2 $\mu mol\ g^{-1}\ h^{-1}$ and 207.2 $\mu mol\ g^{-1}\ h^{-1}$, as illustrated in Figure 10e–h, respectively. These results demonstrated that AgBr/POM/GO ternary composites exhibit noteworthy photocatalytic activity for H_2 generation due to their outstanding redox properties and high capacity for photo-induced electron–hole generation.

TiO_2/graphene oxide was prepared by Wang et al. [133] to overcome the quick recombination problem of photo-generated charge carriers. The as-prepared TiO_2/GO nanocatalyst exhibited enhanced photocatalytic activity compared to pure TiO_2 owing to the larger surface area and that it inhibited the recombination of the charge carriers by accelerating the separation of the photo-carriers. Peng et al. [134] fabricated GO-CdS nanocomposites that exhibited enhanced photocatalytic activity for H_2 generation compared to CdS alone. The H_2 evolution rate of GO-CdS reached as high as 314 $\mu mol\ h^{-1}$. This improved performance was attributed to the coupling of GO with CdS, which effectively accepted and transferred the electrons from the semiconductor, which was beneficial for resisting the recombination of the charge carriers and then enhanced the interfacial charge transfer, which resulted in improved photocatalytic activity. Zn(O,S)/GO heterostructures have been examined for photocatalytic H_2 evolution by Gultom et al. [135]. The highest H_2 evolution rate observed was 2840 $\mu g\ h^{-1}$, which was two-fold superior to Zn(O, S) without GO. GO proved to be an inexpensive and beneficial cocatalyst for Zn(O,S). Designing heterostructures with GO is considered to be a feasible strategy to uplift the photocatalytic performance of the heterostructures as the superior electron conductivity of graphene oxide enables it to effectively accept photo-generated electrons. Consequently, the more efficient separation of photo-induced charge carriers is beneficial to enhance the photocatalytic performance of semiconductors, as proved by the abovementioned results of various GO-based heterostructures.
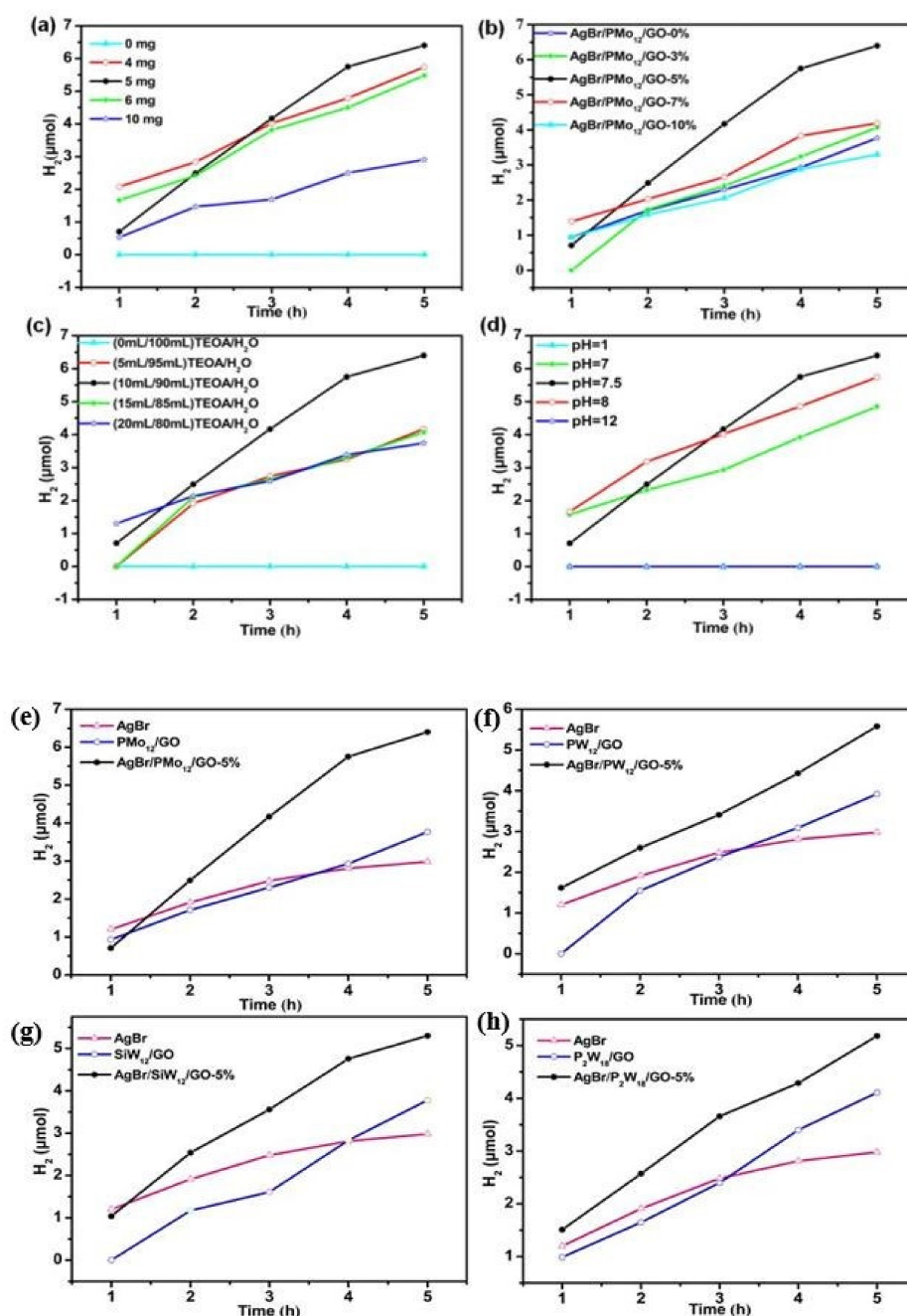
Figure 10. (**a**) Effect of the catalyst quality of $AgBr/PMo_{12}/GO$-5% on hydrogen evolution yields. (**b**) Effect of the amount of AgBr on hydrogen evolution yields. (**c**) Effect of the content of TEOA on hydrogen evolution yields. (**d**) Effect of the pH value on hydrogen evolution yields. Photocatalytic hydrogen evolution experiments of control samples with AgBr/POM/GO-5%. Reaction conditions: 5 mg of composites (**e**) $AgBr/PMo_{12}/GO$-5%, (**f**) $AgBr/PW_{12}/GO$-5%, (**g**) $AgBr/SiW_{12}/GO$-5%, and (**h**) $AgBr/P_2W_{18}/GO$-5% with 100 mL of 10% (V/V) $TEOA/H_2O$ (pH = 7.5) solution. (Reprinted with permission from reference [132]. Copyright 2021, American Chemical Society).

6. Reduce Graphene Oxide as a Photocatalyst

The role of rGO as a catalytic support with the features of an electron acceptor and a transporter in photocatalytic heterostructured systems has been widely studied for H_2 generation via OWS in recent years. When rGO is composited with other semiconductor photocatalysts, it accelerates the effective charge transfer via its conjugated structure and, therefore, suppresses the recombination rate of photo-induced electron–hole pairs. In a work, Wang et al. [136] fabricated and examined $Pt/TiO_2/rGO$ for photocatalytic H_2 gener-

ation. The continuous H_2 generation profile is demonstrated in Figure 11a, and the highest photocatalytic H_2 evolution rate achieved was 1.075 mmol $h^{-1}g^{-1}$ of Pt/TiO$_2$/rGO-2%, which was 81 times higher than TiO$_2$ alone and five times more than Pt/TiO$_2$, as shown in Figure 11b. This excellent photocatalytic outcome was ascribed to the combined effect of TiO$_2$, Pt and rGO, which elevated the transfer of electrons to resist the recombination of photo-excited charge carriers. Because of the excellent photocatalytic activity demonstrated by the as-prepared catalyst Pt/TiO$_2$/rGO-2%, the stability of the compound was examined. Figure 11c,d reveal the photocatalytic stability of the Pt/TiO$_2$/rGO heterostructured photo-catalyst. The schematic fabrication process of the as-prepared nanocomposites is illustrated in Figure 11e.
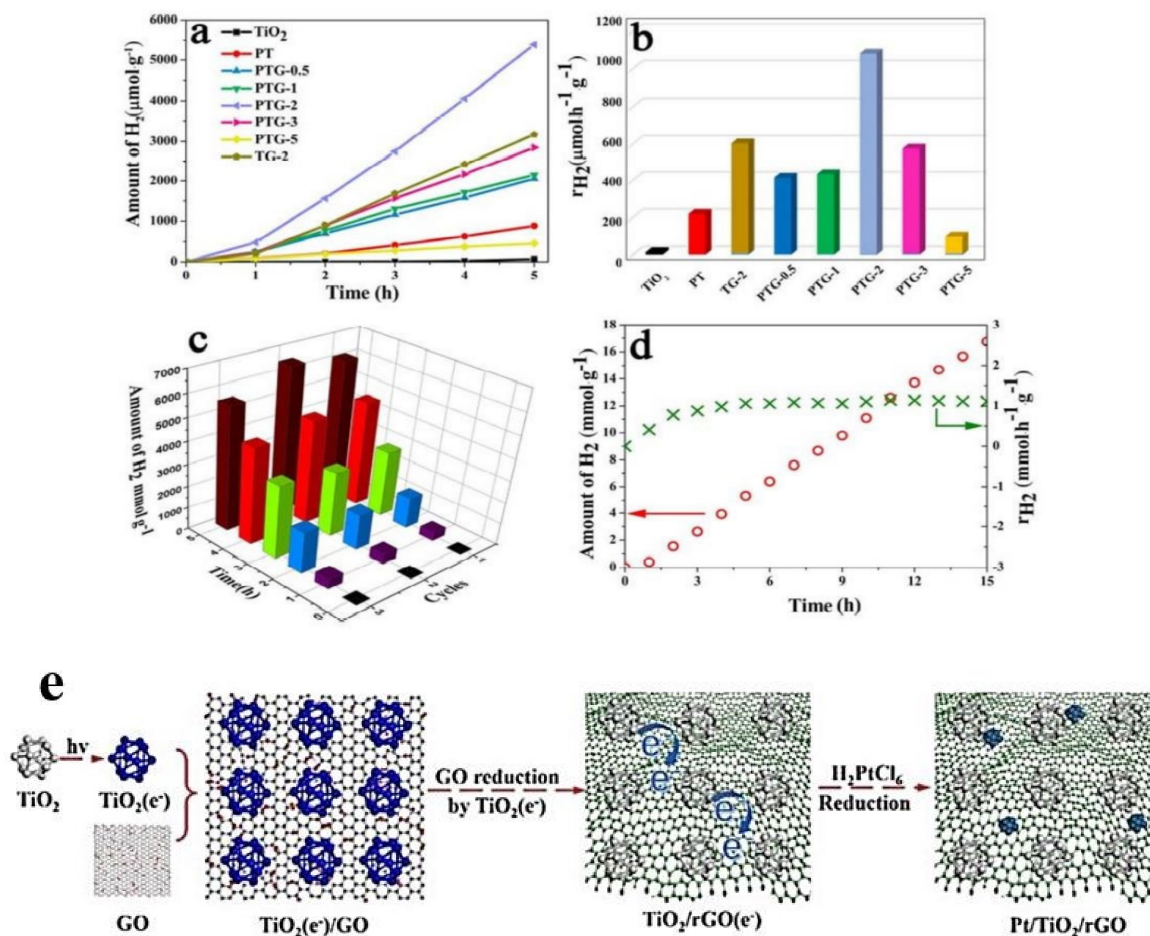

Figure 11. (**a**) H_2 generation profile, (**b**) rate of hydrogen generation for different samples, (**c**) stability study, (**d**) H_2 generation from a continuous measurement for Pt/TiO$_2$/rGO-2%, and (**e**) schematic preparation procedure of Pt/TiO$_2$/rGO nanocomposite. (Reprinted with permission from reference [136]. Copyright 2017, Elsevier).

Wang et al. [137] developed a ZnO/rod-CdS/rGO heterostructure that exhibited almost a four-fold higher photocatalytic H_2 evolution rate than the binary ZnO/rod-CdS heterostructure. The upgraded photocatalytic activity between CdS and ZnO was attributed to the facile charge transfer via rGO nanosheets. In another work, Tran et al. [138] incorporated Cu_2O with rGO in a nanocomposite, employing rGO as an electron acceptor to withdraw photo-excited electrons from the cuprous oxide to deactivate the rapid recombination of the charge carriers. As a result, Cu_2O-rGO exhibited significantly enhanced photocatalytic activity for H_2 generation. A TiO$_2$/In$_{0.5}$WO$_3$/rGO ternary heterostructure was synthesized and compared with bare TiO$_2$ and TiO$_2$/In$_{0.5}$WO$_3$ by Shaheer et al. [139]. The optimized photocatalytic activity was shown by photocatalyst TiO$_2$/2 wt% In$_{0.5}$WO$_3$/0.5 wt% rGO, and the H_2 evolution rate was found to be 309.98 μmol $h^{-1}g^{-1}$, which was 12 times

higher compared to TiO_2 alone and five times greater than $TiO_2/In_{0.5}WO_3$, as revealed in Figure 12a,b, respectively. Further, the stability of the optimized $TiO_2/2$ wt% $In_{0.5}WO_3$ and $TiO_2/2$ wt% $In_{0.5}WO_3/0.5$ wt% rGO photocatalysts was examined, as demonstrated in Figure 12c,d, respectively. This enhanced photocatalytic activity of $TiO_2/In_{0.5}WO_3$ was attributed to the rGO incorporation as it caused the narrowing of the band edge due to the heterojunction formation above the rGO nanosheets that ultimately accelerated the electron–hole pair separation. The S-scheme mechanism of the $TiO_2/In_{0.5}WO_3/rGO$ photocatalyst for H_2 production performance is represented in Figure 12e.

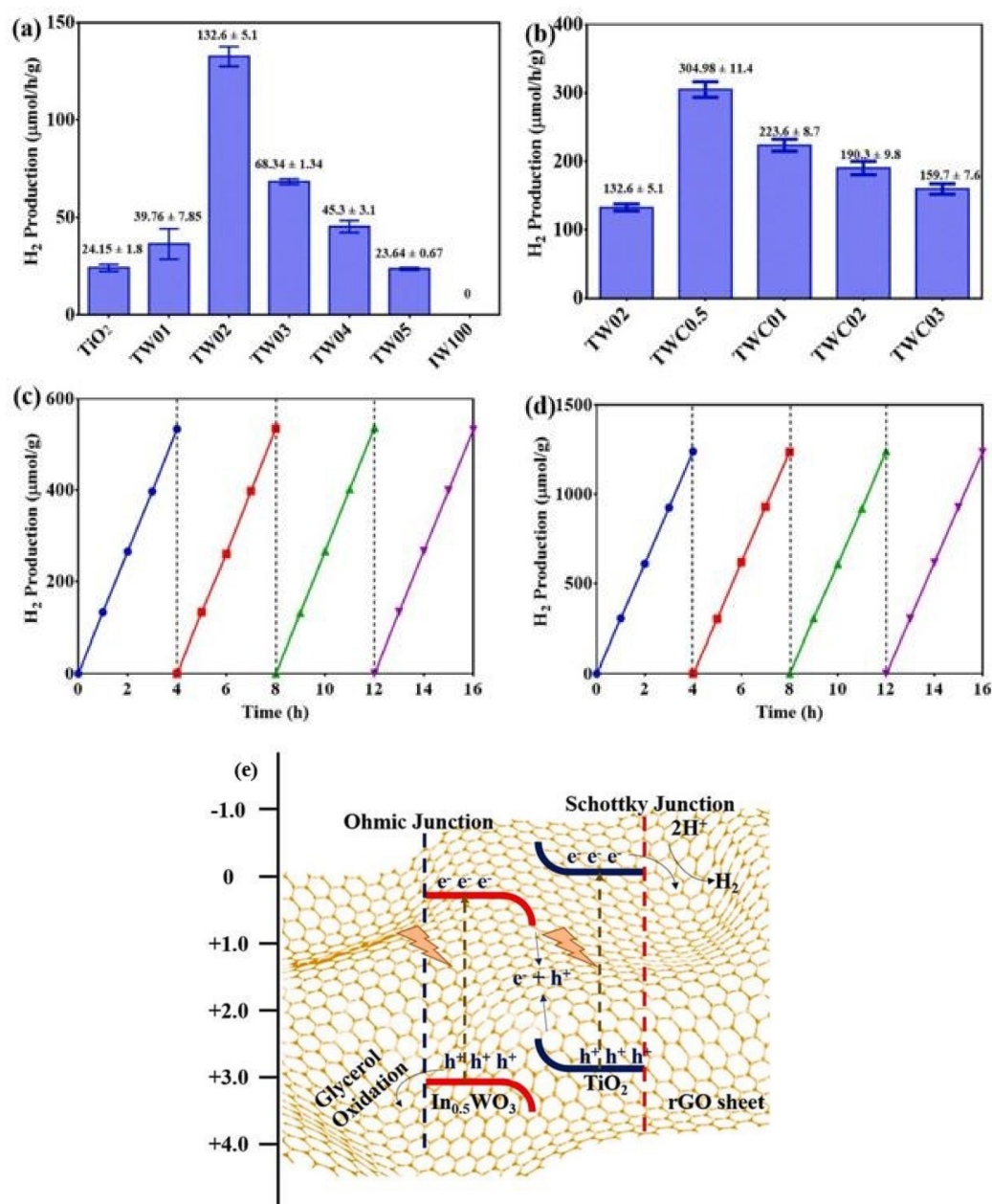**Figure 12.** Photocatalytic H_2 production activity of (**a**) TiO_2, $In_{0.5}WO_3$ and different wt% $In_{0.5}WO_3$ loaded photocatalysts, (**b**) Different wt% rGO loaded $TiO_2/2$ wt% $In_{0.5}WO_3$ photocatalysts, (**c**) Stability test for optimized $TiO_2/2$ wt% $In_{0.5}WO_3$, (**d**) Stability test for rGO optimized photocatalyst $TiO_2/2$ wt% $In_{0.5}WO_3/0.5$ wt% rGO and (**e**) A plausible mechanism for solid state-supported S-scheme photocatalytic H_2 production activity. (Reprinted with permission from reference [139]. Copyright 2021, Elsevier).

Yadav et al. [140] synthesized CuO/rGO binary heterostructures for H_2 production through PWS. The comparative study between bare CuO and CuO/rGO revealed the excellent photocatalytic efficiency of the latter. The H_2 evolution rate of CuO/rGO was 19.2 mmol $h^{-1}g^{-1}$, which was approximately three times higher than bare CuO. He et al. [141] fabricated $SrTiO_3$-rGO for H_2 evolution via PWS. The $SrTiO_3$-rGO exhibited enhanced photocatalytic activity than $SrTiO_3$ alone. This upgraded performance was attributed to resisting rapid charge carrier combination and the increased active sites due to the synergic effect of rGO with $SrTiO_3$. Xue et al. [142] designed $rGO/Cd_{0.5}Zn_{0.5}S/g$-C_3N_4 photocatalytic systems for H_2 generation. The $rGO/Cd_{0.5}Zn_{0.5}S/g$-C_3N_4 ternary heterostructures showed a H_2 production rate as high as 39.24 mmol $g^{-1}h^{-1}$, which was much better than $Cd_{0.5}Zn_{0.5}S$ alone and pristine g-C_3N_4. This effective result was attributed to the combined out-turn between g-C_3N_4 and $Cd_{0.5}Zn_{0.5}S$ in the presence of rGO, which played key role as an intermediary of the charge carriers in between two semiconductors. The nanocomposites $GO/ZnIn_2S_4$ were prepared and examined by Ye et al. [143] for photocatalytic H_2 production. The $rGO/ZnIn_2S_4$ nanocomposites exhibited improved photocatalytic activity for H_2 generation, which was ascribed to the synergistic effect of rGO with $ZnIn_2S_4$. Hafeez et al. [144] prepared an rGO-supported g-C_3N_4-TiO_2 ternary photocatalyst and investigated it in relation to its photocatalytic performance for H_2 generation. The g-C_3N_4-TiO_2/rGO nanocomposites exhibited massive 23,143 mmol $g^{-1}h^{-1}$ H_2 production activity, which was 78 times more than pristine g-C_3N_4 and 2.5 times higher than TiO_2 alone. The enhanced outcomes were credited to the extended absorption in visible light and the efficient segregation of photo-excited charge carriers. A study on the photocatalytic activity for H_2 generation of rGO/CdS was reported by Zeng et al. [145]. The rGO/CdS showed much better photocatalytic performance for H_2 production, which was ascribed to the suppression of the rapid recombination of photo-induced charge carriers by rGO.

All of these research successes infer that for improvising the photochemical response of photocatalysts, rGO has been employed as a support material in binary and ternary photocatalytic systems owing to numerous advantages, including considerable adsorption sites due to its higher specific surface area, proclivity to suppress the recombination rate of photo-generated electron–hole pairs, the band edge attenuation of semiconductors and its ability to impede the rate of photo-corrosion. These features mold it into an appreciable material in the area of visible-light-driven PWS technology, which has also been corroborated by the aforementioned reports of binary and ternary rGO-based heterostructured photocatalysts. The catalytic efficiency of graphene and its derivative-based photocatalysts is summarized in Table 3.

Table 3. Photocatalytic activity of graphene and its derivatives based photocatalysts.

Photocatalyst	Synthetic Route	Light Source/Photo Conversion Efficiency	Sacrificial Agent	Band Gap (eV)	H_2 Evolution Performance	Ref.
Ag-TiO_2/graphene	Microwave-assisted hydrothermal	300 W Xenon Lamp	Methanol/Water	~2.8	225 µmol h^{-1} g^{-1}	[116]
CdS/graphene nanoribbons	Solvothermal	300 W Xenon Lamp	Lactic acid	2.17	1.891 mmol $h^{-1}g^{-1}$	[117]
CdS/MoS_2/graphene	Biomolecule assisted	300 W Xenon Lamp	Lactic acid/Water	-	1913 µmol h^{-1} g^{-1}	[118]
CdS/Nb_2O_5/N-doped graphene	Hydrothermal	150 W Xenon Lamp	Na_2S/Na_2SO_3	2.0	800 µmol g^{-1}	[119]
Eu-TiO_2/graphene	Sol-gel/Hydrothermal	Metal Halogen Lamp	Na_2S/Na_2SO_3	-	100 mmol h^{-1} g^{-1}	[120]
Ni-doped ZnS-graphene	Solvothermal	300 W Mercury Lamp	Na_2S/Na_2SO_3	-	8683 µmol h^{-1} g^{-1}	[121]
WS_2/Graphene-CdS	Solvothermal	500 W Xenon Arc Lamp	Na_2S/Na_2SO_3	2.4	1842 µmol h^{-1} g^{-1}	[122]
ZnO-ZnS/graphene	Calcination/Deposition	300 W Mercury Lamp	Glycerol	3.35	1070 µmol h^{-1} g^{-1}	[123]
Graphene QDs/TiO_2	Hydrothermal	Natural Solar Light/9.84%	Glycerol	2.72	29548 µmol h^{-1} g^{-1}	[124]
GO-CdS-Pt	Reduction	400 W Mercury Lamp	Methanol	-	123 mL $h^{-1}g^{-1}$	[126]
GCN/ACN/GO	Soft grafting	Xenon Arc Lamp	Triethanolamine	2.55–2.60	251 µmol h^{-1}	[127]

Table 3. *Cont.*

Photocatalyst	Synthetic Route	Light Source/Photo Conversion Efficiency	Sacrificial Agent	Band Gap (eV)	H$_2$ Evolution Performance	Ref.
S-GO QDs	Hydrothermal	500 W Xenon Lamp	Ethanol	2.34	30,519 μmol h^{-1} g^{-1}	[128]
GO-C$_3$N$_4$-LaVO$_4$	Hydrothermal	300 W Xenon Lamp	Na$_2$SO$_4$	-	717.6 μmol h^{-1}g^{-1}	[129]
Pt/GO-ZnS	Hydrothermal/ Deposition	300 W Xenon Lamp	Lactic acid	3.34	1082 μmol h^{-1} g^{-1}	[130]
N-doped TiO$_2$/ graphene oxide	Hydrothermal	500 W Mercury Lamp	Methanol/Water	2.69	716 μmol h^{-1} g^{-1}	[131]
TiO$_2$/graphene oxide	Sol-gel/Calcination	550 W Xenon Lamp	Methanol/Water	2.43	0.321 mmol g^{-1}h^{-1}	[133]
GO-CdS	Precipitation	300 W Xenon Lamp	Na$_2$S/Na$_2$SO$_3$	-	314 μmol h^{-1}	[134]
Zn(O,S)/GO	Co-precipitation	UV Lamp	Ethanol/Water	-	2840 μg h^{-1}	[135]
Pt/TiO$_2$/rGO	Photo-reduction	Solar Simulator	Triethanolamine	2.76	1075.68 μmol h^{-1} g^{-1}	[136]
ZnO/rod-CdS/rGO	Light irradiation	300 W Xenon Lamp	Na$_2$S/Na$_2$SO$_3$	-	0.59 mmol h^{-1}	[137]
Cu$_2$O-rGO	Co-precipitation	150 W Xenon Lamp/18%	Methanol/Water	-	264.5 μmol g$_{cat}$$^{-1}$ h^{-1}	[138]
TiO$_2$/In$_{0.5}$WO$_3$/rGO	Wet impregnation/ Hydrothermal	Xenon Arc Lamp	Glycerol	3.02	304.98 $\pm$ 11.4 μmol h^{-1} g^{-1}	[139]
CuO/rGO	Hydrothermal	300 W Xenon Lamp	Methanol	-	19.2 mmol h^{-1} g^{-1}	[140]
SrTiO$_3$-rGO	Hydrothermal	300 W Xenon Lamp	Methanol	3.03	363.79 μmol h^{-1} g^{-1}	[141]
rGO/Cd$_{0.5}$Zn$_{0.5}$S/g-C$_3$N$_4$	Hydrothermal	Xe Lamp	Na$_2$SO$_4$	-	39.24 mmol h^{-1}g^{-1}	[142]
rGO/ZnIn$_2$S$_4$	Solvothermal	300 W Xenon Lamp	Lactic acid	2.4	40 μmol h^{-1}	[143]
g-C$_3$N$_4$-TiO$_2$/rGO	Wet impregnation	250 W Xenon Lamp	Glycerol/Water	2.56	23143 μmol h^{-1}g^{-1}	[144]
rGO/CdS	Solvothermal	300 W Xenon Lamp	Na$_2$S/Na$_2$SO$_3$	2.03	420 μmol h^{-1}	[145]

7. Electrochemical H$_2$ Production

The H$_2$ generation process via EWS is an eminently propitious approach for resolving the energy crisis and environmental pollution problems [146–148]. The requirement of the electrical energy for electrocatalysis is generally fulfilled by photovoltaic cells that generate electricity directly from solar light [149]. EWS operation includes both half-cell reactions for OER and HER. For that, an electrolysis cell contains two electrodes that are dipped in an electrolyte suspension. The current starts to flow from an anode, which is a positive electrode, to a cathode, which is a negative electrode, when the direct current source is attached to the electrodes. Thereby, the water that is in the electrolyte splits into H$_2$ from the negative electrode (Half reaction at the cathode: $2H_2O + 2e^- \rightarrow H_2 + 2OH^-$) and oxygen from the positive electrode (Half reaction at the anode: $4OH^- \rightarrow 2H_2O + O_2 + 4e^-$). For overall EWS (H$_2$O + electric current $\rightarrow$ H$_2$ + 1/2 O$_2$ + heat), the electrode surface (cathode) is an essential parameter for effective H$_2$ production. Hydrogen evolution reaction (HER) is commonly considered a two-electron migration process, which is one of the intermediaries of the adsorption–desorption method. On the electrocatalyst surface, one proton adsorbs succeeded by the deduction of one electron, resulting in the H* adsorbed intermediate (*showing the adsorbed active site), which is known as the Volmer step. Successively, the H* couples with H$^+$ and removes one electron, which leads to the production of one H$_2$ molecule, known as the Heyrovsky step. On the other hand, in the Tafel step, the adsorbed H* tends to combine with another H* to form a H$_2$ molecule under a higher range of surrounding H*. Unlike the two-step process in acidic media, on the surface, the adsorbed H$_2$O begins to dissociate at the start of HER because of the proton presence in the alkaline medium. Hence, H$_2$ can be generated through the coupling of H* with a H$_2$O molecule. The oxygen evolution reaction (OER) follows the four-electron transfer method with a number of intermediates. The variation in the total free energy of OER is found to be 4.92 eV. Generally, platinum-based catalysts are the most conventionally equipped cathodes for EWS. Platinum is a very expensive material, and consequentially, electrolysis is the simplest method, but woefully it is not cost-effective. To overcome this obstacle, the development of economical, stable and highly efficient catalysts is needed for H$_2$ evolution via EWS [150–152].

One of the pioneering, trail-blazing approaches to overcoming the cost barrier is the utilization of lucrative graphene and its derivative-based binary and ternary heterostructures, which are much cheaper, have extremely high surface areas and excellent electrical

conductivity. In addition, their declined Tafel slope and overpotential values make a strong case for their application as advanced electrocatalysts. There are many fascinating studies that have reported on exploiting graphene and its derivatives as supporting materials for EWS, stressing their scalability, as discussed below. Zhang et al. [153] fabricated an rGO-incorporated transition metal phosphide (TMP) electrocatalyst. They successfully doped O into resulting TMPs through pyrolyzing phytic acid crosslinked complexes and then incorporated them within the rGO nanosheets, as depicted in Figure 13a–e. The resultant configuration widened the bonds of metal-P and accelerated the intrinsic conductivity of metal phosphides, which manifested its tremendous electrocatalytic activity. The HER results of the rGO-incorporated MoP hybrid in the alkaline and acidic mediums required a small overpotential of 93 mV and 118 mV to achieve a current density of 20 mA cm^{-2}, respectively, as demonstrated in Figure 13f,g.
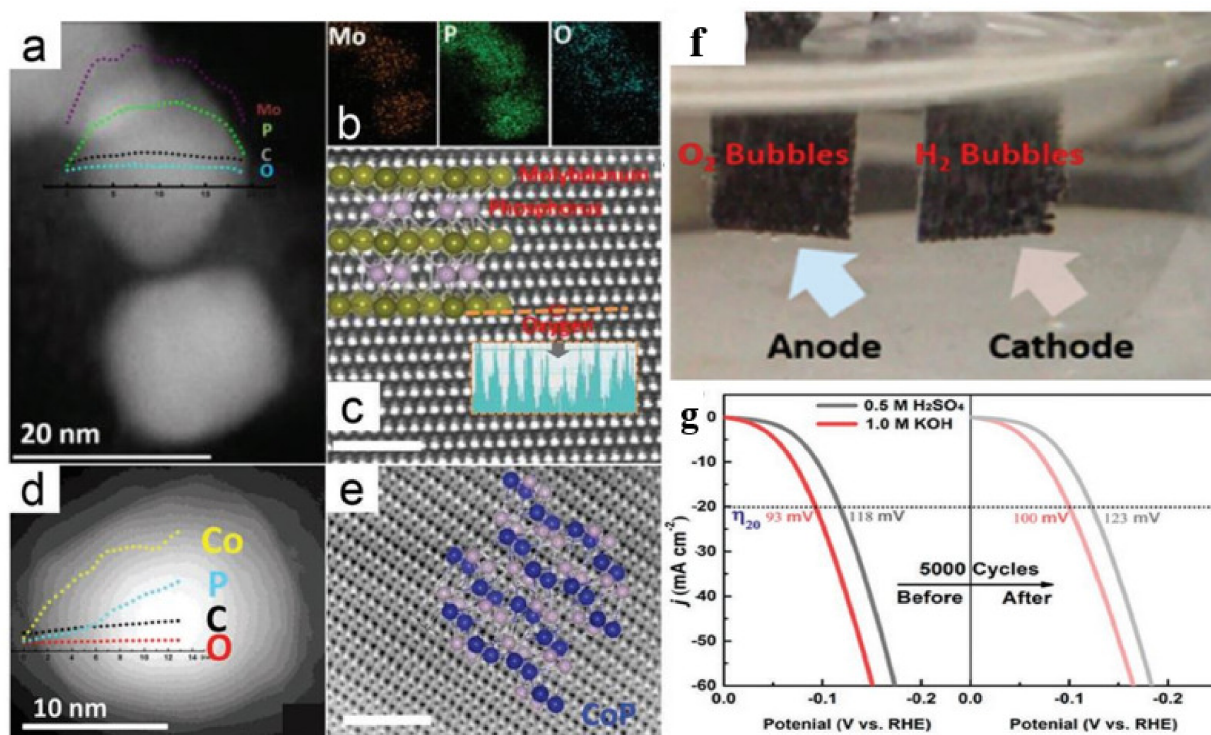

Figure 13. (**a**) STEM image of MoP nanoparticles. Inset: intensities for different elements. (**b**) Large area STEM-EDS mapping to Figure 13a. (**c**) HAADF-STEM image of MoP with the corresponding crystal structure superimposed. The intensity profile along orange dashed line directly shows the presence of O atoms. (**d**) The STEM image of CoP. Inset: the intensities of the elements present in particles. (**e**) HAADF-STEM image of CoP with the crystal structure superimposed. Scan bars, 1 nm. (**f**) Optical photograph showing the generation of bubbles on the MoP- and CoP-based electrodes. (**g**) Polarization curves of MoP measured both in 0.5 M H$_2$SO$_4$ and 1 M KOH (left) and curves after 5000 potential sweeps at 20 mV·s^{-1} (right), without iR-drop corrections. (Reprinted with permission from reference [153]. Copyright 2016, American Chemical Society).

In another study, Xu et al. [154] prepared penroseite (Ni,Co)Se$_2$ nanocages utilizing analogs of Prussian blue as the precursor and then anchored them on a 3D graphene aerogel (GA), as illustrated in Figure 14a–h. The special morphology of (Ni,Co)Se$_2$ nanocages offered a number of active sites, and during the vigorous binding between GA and (Ni,Co)Se$_2$, it accelerated the charge transfer and improved their interfacial contact. (Ni,Co)Se$_2$-GA electrocatalyst demanded a small overpotential of 128 mV to obtain a 10 mA cm^{-2} current density, which was effectively smaller than the (Ni,Co)Se$_2$ and GA catalysts, as revealed in Figure 14i–k.
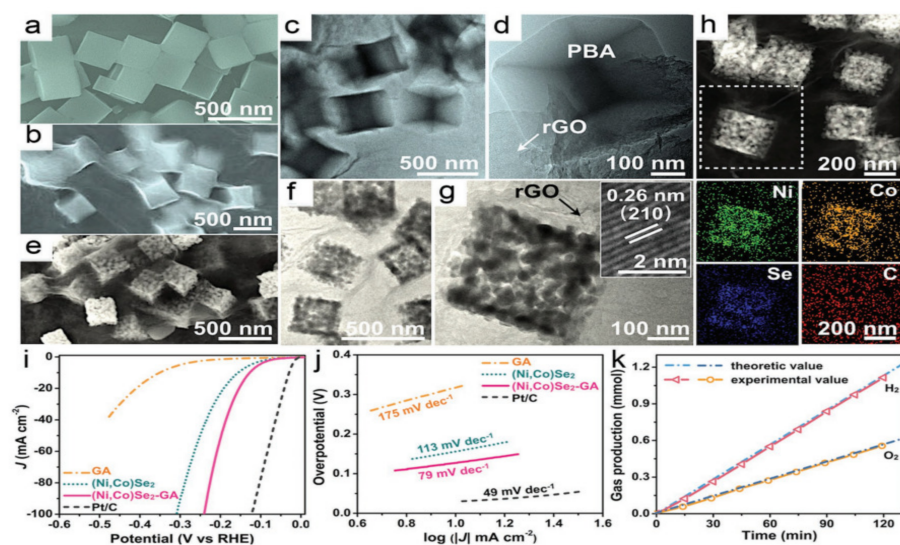
Figure 14. (**a**) SEM image of NiCo PBA nanocubes. (**b**) SEM and (**c**,**d**) TEM images of NiCo PBA-GA. (**e**) SEM, (**f**,**g**) TEM images, and (**h**) HADDF image and the corresponding elemental maps of $(Ni,Co)Se_2$-GA. The inset of (**g**) shows the HRTEM image of $(Ni,Co)Se_2$-GA. (**i**) IR-corrected HER polarization curves of $(Ni,Co)Se_2$-GA (**j**) Corresponding Tafel plots. (**k**) H_2 and O_2 production catalyzed by $(Ni,Co)Se_2$-GA in 1 m KOH at room temperature. (Reprinted with permission from reference [154]. Copyright 2017, American Chemical Society).

8. Graphene as Electrocatalyst

As a salient member of the carbon family, graphene, with its considerable features, has captivated noteworthy and tenacious attention. However, bare graphene having significant graphitization is inert electrochemically and possesses comparatively low HER activity. A number of chemical modifications have been reported for the betterment of its catalytic performance as an electrocatalyst, as discussed through some visionary reports here. Fei et al. [155] reported Co-Nitrogen doped Graphene (Co-NG) electrocatalyst for H_2 generation. The electrocatalyst demonstrated an excellent electrochemical response, with a small overpotential of 30 mV and a Tafel slope value of 82 mV dec^{-1}. The outstanding catalytic activity, scalability and cost-effectiveness of the Co-NG electrocatalyst make it an optimistic substitute for Pt. Subramanya et al. [156] fabricated a Co-Ni-Graphene(Co-Ni-G) electrocatalyst to investigate the electrocatalytic efficiency of an as-prepared ternary heterostructure for H_2 generation. The Tafel slope obtained was 84.5 mV dec^{-1} at 40 mA cm^{-2}, and the highest current density reached 850 mA cm^{-2} (at 1.6 V), which was about four-fold higher than a Co-Ni binary alloy, indicating the beneficial incorporation of graphene, which significantly increased the active surface area and enhanced the catalytic performance for H_2 generation. An Fe-Ni-Graphene composite was prepared by Badrayyana et al. [157] for electrochemical H_2 evolution. The Tafel slope was observed to be 88.1 mV dec^{-1}, which implied the rapid adsorption/desorption rate of HER, and the exchange current density was found to be 284.5 µA cm^{-2}, which was nearly thrice that of an Fe-Ni binary alloy. This improved catalytic performance for H_2 generation was attributed to the embedding of graphene on the Fe-Ni alloy, which increased its electrochemically active surface area. Huo et al. fabricated an Mo_2C/Graphene [158] electrocatalyst for H_2 production, and the as-designed electrocatalyst yielded excellent catalytic efficiency toward HER. The Mo_2C/Graphene showed a very low overpotential of 8 mV with a Tafel slope of 58 mV dec^{-1}, which was ascribed to the acceleration in the rate of charge transfer and a higher electrochemically active surface area. Han et al. [159] reported the synthesis of an Ni_2P-G@NF electrocatalyst (nickel phosphide on graphene/nickel foam) for H_2 generation via EWS. Ni_2P-G@NF demonstrated superior performance for electrocatalytic H_2 generation, with a 7 mV overpotential in an alkaline situation. The excellent results were ascribed to the large surface area and the rapid electron transfer rate. Li et al. [160] fabricated an

Ni/Mo$_2$C@C (Ni/Mo$_2$C with graphene) electrocatalyst for effective H$_2$ generation. The as-prepared electrocatalyst showed noteworthy performance with long-time-span stability, which corresponded to the combined effect between Mo$_2$C, Ni and graphene together. Huang et al. [161] prepared a Nitrogen-doped mesoporous Graphene (N-MPG) electrocatalyst for H$_2$ evolution, in which the Tafel slope was obtained to be 109 mV dec^{-1}. The as-prepared electrocatalyst demonstrated efficient electrocatalytic activity for HER owing to the remarkable current density and outstanding stability. The excellent performance was attributed to the synergistic effect between Ni/Mo$_2$C and graphene that enhanced the electrochemical H$_2$ generation. Figure 15 shows the schematic demonstration for the synthesis of mesoporous graphene.
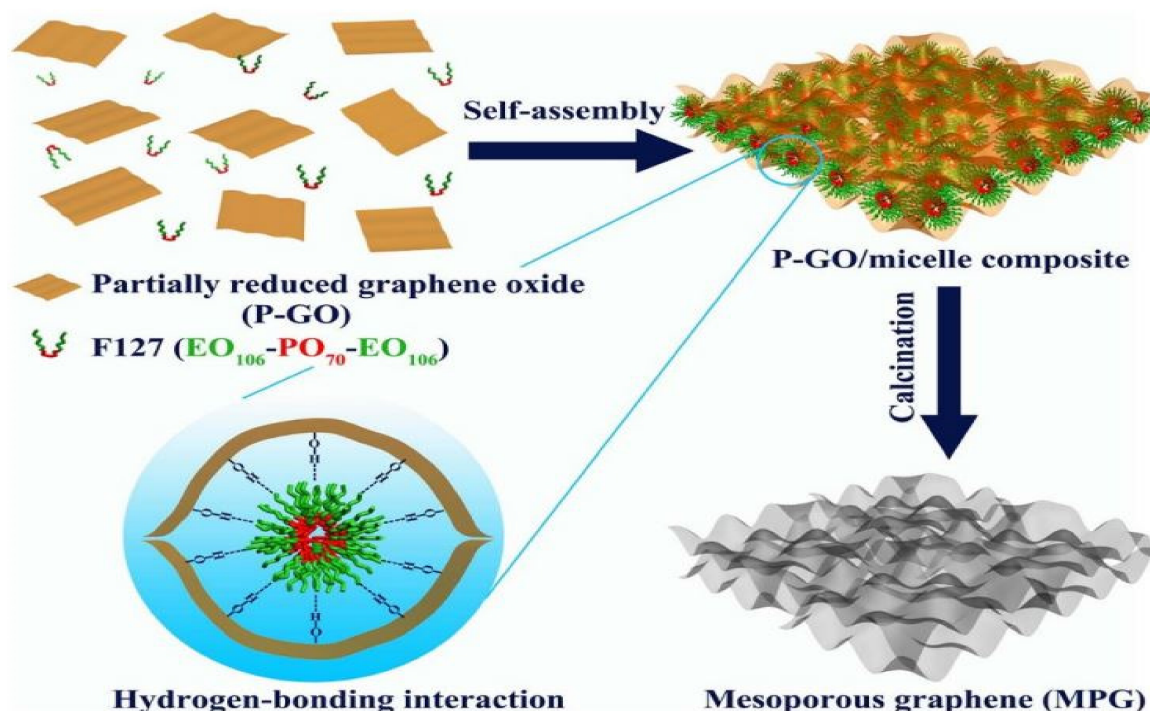

Figure 15. Schematic illustration for preparing mesoporous graphene. (Reprinted with permission from reference [161]. Copyright 2014, Nature Publishing Group).

A Pd/Graphene nanocomposite was fabricated and investigated by Ghasemi et al. [162] for electrocatalytic H$_2$ evolution. The Pd/Graphene electrocatalyst demonstrated effective results for H$_2$ generation, with a lower Tafel slope value of 46 mV dec^{-1}, which was a much greater catalytic performance than pristine Pd and graphene electrocatalysts. These results proved that graphene is an outstanding support catalyst for H$_2$ generation via EWS. The encouraging quantum leaps of cost-effective graphene-based electrocatalysts as a promising replacement of costly nanomaterials towards efficient HER is substantiated by the aforementioned results. It is effortless to perceive that graphene-based cost-effective heterostructures are dynamic and stable electrocatalysts, which are envisaged for scalable H$_2$ production.

9. Graphene Oxide as Electrocatalyst

For efficient H$_2$ production through EWS by employing GO-based heterostructures, extensive research has been widely undertaken in recent years. Zhou et al. [163] fabricated an MoS$_2$/GO binary heterostructure for EWS. The MoS$_2$/GO exhibited noticeable electrochemical performance for HER, carrying a very small overpotential (107 mV) and Tafel slope (86.3 mV dec^{-1}). This accelerated performance was ascribed to the synergistic effect of MoS$_2$ and GO, where GO has provided a higher number of active sites. Cu$_2$ZnSnS$_4$ (CZTS)/GO heterostructured nanocatalyst was fabricated by Digraskar

et al. [164] to examine the electrocatalytic activity for HER. As a result, it was revealed to be an efficient electrocatalyst with a high current density of 908 mA cm^{-2} and a low overpotential of 53.1 mV. The enhanced catalytic activity was mainly attributed to the incorporation of GO, which accelerated the charge transfer rate, improving the H$_2$ evolution performance. In another study, Narwade et al. [165] reported the synthesis of an Rh-GO nanocatalyst, which exhibited significantly enhanced electrocatalytic activity for HER, with a very small overpotential of 2mV and a 10 mV dec^{-1} Tafel slope. This result was attributed to the decoration of rhodium nanoparticles on GO, which led to facilitating interfacial electron transfer. Hu et al. [166] prepared MoS$_x$/GO with different oxidation degrees of GO, denoting GO1, GO2 and GO3, which showed excellent electrocatalytic activity for HER. The highest electrocatalytic activity for HER with an onset potential of 0.1 V was exhibited by MoS$_x$/GO2, as represented in Figure 16a. The optimal electrochemical activity of MoS$_x$/GO2 reached a small overpotential (195 mV) and nearly a 47.7 mV dec^{-1} Tafel slope, and the largest active surface area was possessed by MoS$_x$/GO2, as demonstrated by the Tafel plot and impedance spectra in Figure 16b,c, respectively. For each active site, the TOF of MoS$_x$/GO2 was calculated as 0.94 s^{-1}, which was much better than other samples, as revealed in Figure 16d. The enhanced electrochemical activity for HER was ascribed to the enhanced conductivity and dispersion of GO in MoS$_x$.
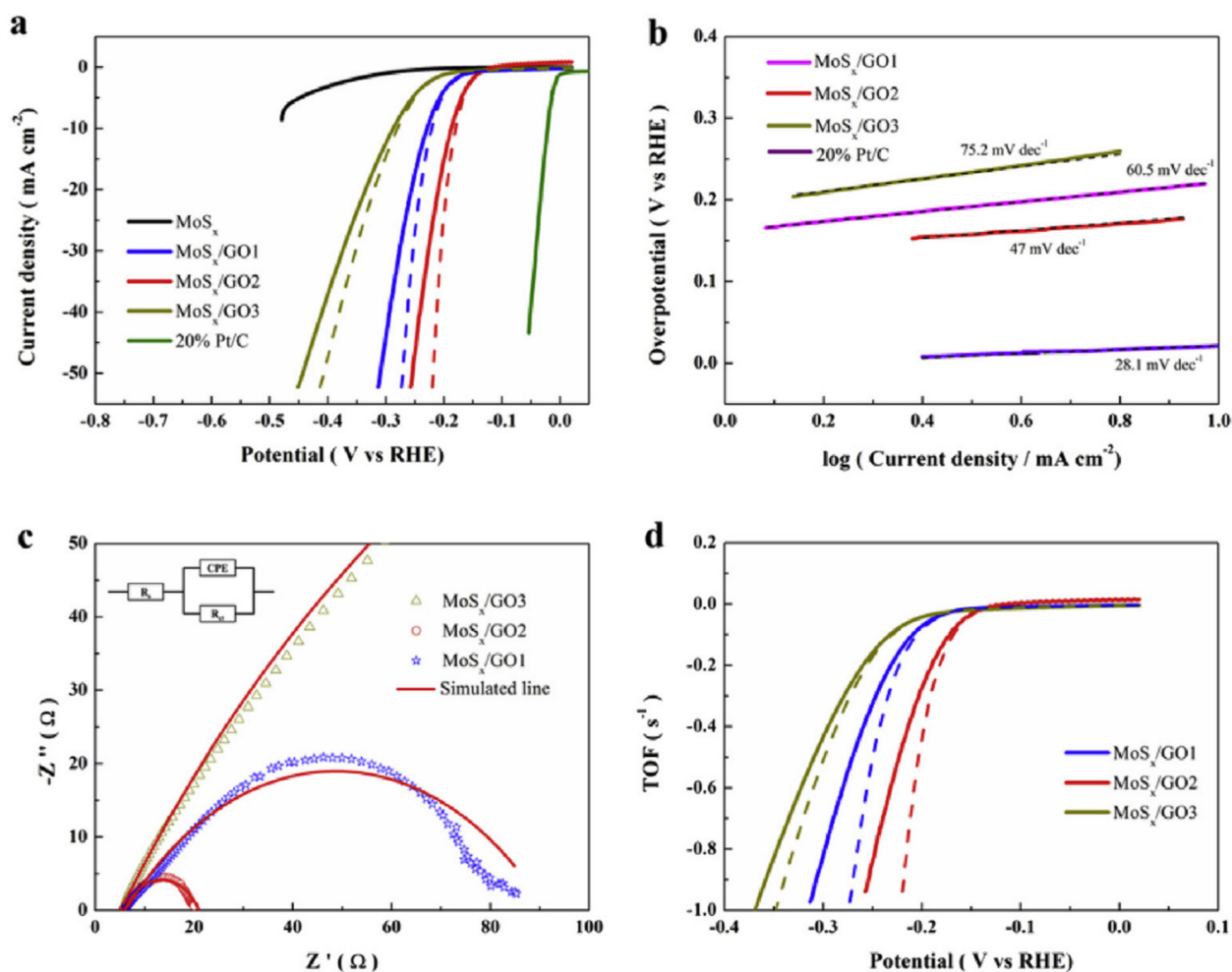

Figure 16. (**a**) Linear sweep voltammogram curves in 0.5M H$_2$SO$_4$ for different MoS$_x$/GO electrocatalysts; (**b**) Tafel plots of different MoS$_x$/GO electrocatalysts; (**c**) AC impedance spectra for different MoS$_x$/GO electrocatalysts; (**d**) Calculated turnover frequencies of different MoS$_x$/GO electrocatalysts, the dashed line is the TOF curve with iR correction. (Reprinted with permission from reference [166]. Copyright 2016, Elsevier).

Graphene Oxide coated with Nickel foam (GO@Ni) was fabricated by Sarawutanukul et al. [167] to examine the electrocatalytic efficiency for H_2 evolution. The as-engineered electrocatalyst exhibited excellent results, with a 55.7 mV Tafel slope and an 83.2 mV overpotential, which was much better than pristine Ni foam. The superior catalytic activity was attributed to the synergistic effect between GO and Ni foam. Fu et al. [168] synthesized $Ni_{0.85}Se$/N-Graphene Oxide nanocomposites for electrocatalytic H_2 generation. The robust contact between N-Graphene Oxide (N-GO) and $Ni_{0.85}Se$ demonstrated efficient electron transfer, which resulted in excellent HER performance, showing low overpotential (104 mV) and a small Tafel slope (50.7 mV dec^{-1}). Lotfi et al. [169] developed a Platinum/Graphene Oxide/Nickel-Copper/Nickel Foam (Pt/GO/Ni-Cu/NF) electrocatalyst for H_2 generation through water splitting. The Pt/GO/Ni-Cu/NF electrocatalysts revealed superior electrochemical activity and advanced stability. The overpotential obtained was 31 mV at 10 mA cm^{-2}, and the Tafel slope was 51 mV dec^{-1}, which was attributed to the elevated electrochemically active surface area due to the introduction of GO, which enhanced the HER performance of the Pt/GO/Ni-Cu/NF electrocatalyst. Theerthagiri et al. [170] synthesized FeS_2/GO heterostructures to investigate their catalytic efficiency toward H_2 generation via EWS. The optimum FeS_2/GO electrocatalyst achieved a low overpotential value of 250 mV and 64 mV dec^{-1} for the Tafel slope. The efficient HER performance was ascribed to the synergistic effect of FeS_2 and GO, which resulted in an abundance of electroactive sites and an acceleration in the charge transfer rate. These results imply that the addition of GO to primary electrocatalytic systems is favorable to magnifying the electrochemical performance and extending the lifespan of electrocatalysts. The enormously inspiring results of GO-based electrocatalysts for H_2 generation through EWS make it an excellent precursor of sustainable energy solutions.

10. Reduced Graphene Oxide as Electrocatalyst

Owing to the diverse structural features of GO, there is a wide array of physicochemical modifications that can be undertaken in order to improve its electrical properties. One such alteration is the reduction of GO, which galvanizes it in order to augment its electrical conductivity, increases the specific surface area and enhances the optoelectronic properties. Reduced graphene-oxide-based binary and ternary heterostructures have exhibited phenomenal results, which sets their course as ameliorated electrocatalysts for H_2 generation through EWS. Chen et al. [171] prepared nano and micro- FeS_2/rGO heterostructures for the investigation of the electrochemical activity for HER. The nano-FeS_2/rGO showed tremendous improvement for HER, reaching a low overpotential (139 mV) and Tafel slope (66 mV dec^{-1}), with remarkable prolonged stability for 100 cycles with trivial deterioration and at a constant overpotential (70 mV) catalyzed continuous H_2 generation. As illustrated in Figure 17a–d. The Gibbs free energy of FeS_2/rGO was also examined, which revealed that the HER activity was exhibited by all of the FeS_2 surface sites, as demonstrated in Figure 17e. The strong interfacial contact between FeS_2 and rGO was the driving force behind the excellent HER electrochemical performance of nano-FeS_2/rGO.

A W-Mo-O/rGO nanocomposite was fabricated by Imran et al. [172] and analyzed for electrochemical performance towards HER. The results manifested a lower onset potential of 50 mV and a Tafel slope of 46 mV dec^{-1} with a sublime lifetime span. The durability and enhanced HER performance stemmed from the synergistic effect of W-Mo-O with rGO. Ma et al. [173] synthesized a CoP/rGO electrocatalyst and examined the HER activity. The CoP/rGO exhibited improved electrocatalytic activity, having a small Tafel slope of 104.8 mV dec^{-1}. This improvement was ascribed to the plentiful electrochemically active sites and enhanced electrocatalytic conductivity of the CoP/rGO nanocomposite.

The pristine NiS_2 and NiS_2/rGO heterostructures were prepared by Chen et al. [174] for the relativistic study of HER electrocatalytic performance. NiS_2/rGO exhibited superior HER performance compared to bare NiS_2. This enhanced electrocatalytic activity for HER was due to the abundant active sites and synergistic effect between NiS_2 and

rGO. Liu et al. [175] synthesized a Co-Ni-P/rGO ternary electrocatalyst for HER performance through EWS. This ternary heterostructured electrocatalyst exhibited noteworthy HER performance, with a 207 mV overpotential. This improved electrocatalytic activity was attributed to the compilation effect and the larger surface area. An Au-Pd/rGO electrocatalyst was prepared by Darabdhara et al. [176] to evaluate the HER response. The outcomes demonstrated that the achieved onset potential was as low as 0.8 mV and the Tafel slope was 29 mV dec^{-1} with high durability. The improved results were due to the remarkably enhanced electrocatalytic conductivity, higher surface area and augmented active site availability. Ojha et al. [177] designed MoP/rGObinary heterostructures for electrochemical H_2 generation. The as-prepared electrocatalyst showed remarkable electrocatalytic performance, with a 42 mV dec^{-1} Tafel slope. In another study, P-MoS$_2$/N,S-rGO heterostructures were reported by Guruprasad et al. [178] for H_2 production via EWS. The as-fabricated electrocatalysts exhibited significantly enhanced electrocatalytic performance toward H_2 production, with a 47 mV Tafel slope and a small overpotential (94 mV), which was ascribed to the combined effect of P-MoS$_2$ with N- and S-doped rGO. Chen et al. [179] synthesized CoP/rGO electrocatalyst for H_2 production. The as-synthesized electrocatalyst demonstrated remarkable electrocatalytic performance toward HER, with an overpotential of 36.6 mV and a 43.1 mV dec^{-1} Tafel slope.
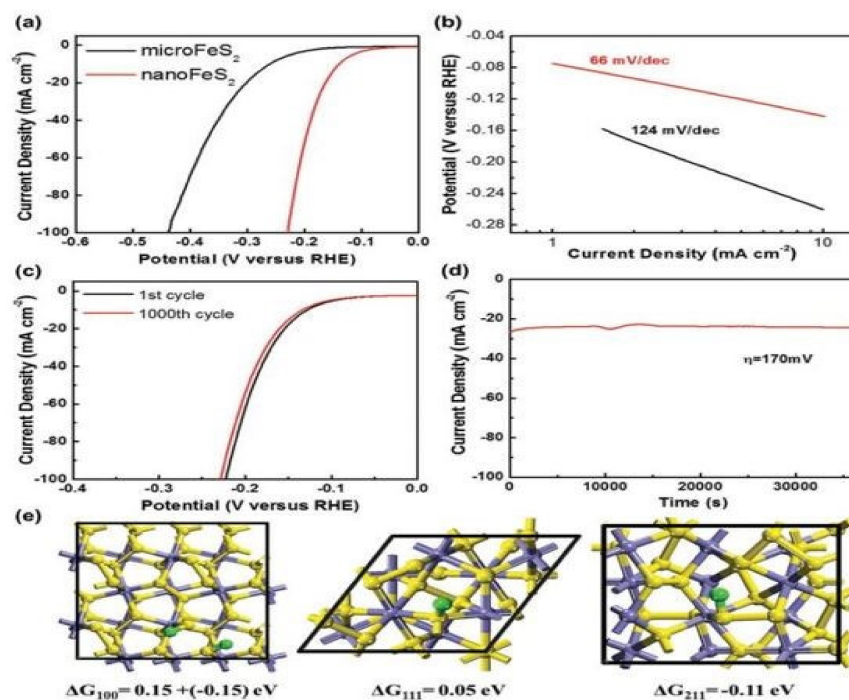

Figure 17. HER electrocatalytic performance of FeS$_2$ nanoparticles. (**a**) The HER polarization curves of nano-FeS$_2$-RGO in comparison to micro-FeS$_2$-RGO at 2 mV s^{-1} in 0.5 m H_2SO_4. (**b**) Corresponding Tafel slopes. (**c**) Cycling stability of nano-FeS$_2$-RGO after continuous potential sweeps at a scan rate of 50 mV s^{-1} in 0.5 m H_2SO_4. (**d**) Time-dependence of the cathodic current density of nano-FeS$_2$-RGO during electrolysis under a constant overpotential of 170 mV in 0.5 m H_2SO_4. (**e**) The configurations of hydrogen adsorption on the different FeS$_2$ surfaces (left (100), middle (111), and right (211)) and the corresponding free energy. In the case of (100), there are two equal S-sites for the HER process, and the free energies are 0.15 and −0.15 eV for the first and second hydrogen. The black boxes denote the used supercells. (Reprinted with permission from reference [171]. Copyright 2017, John Wiley and Sons).

Among discrete electrocatalytic systems, it is predicted that rGO-based electrocatalysts are immensely uncovering electrolytic water applications and widely capturing the attention of researchers because of their intrinsic features. Appreciable development has been made in the exploitation of non-precious rGO-based heterostructures toward HER, as

confirmed by the abovementioned results. The catalytic efficiency of some of the graphene derivative-based electrocatalysts are summarized in Table 4.

Table 4. HER activity by graphene and its derivatives based electrocatalysts.

Electrocatalyst	Electrolyte	Overpotential/Onset Potential	Tafel Slope (mV dec^{-1})	Stability	Ref.
Co-Nitrogen doped Graphene	0.5 M H_2SO_4	30 mV	82	10 h, 1000 CV	[155]
Co-Ni-Graphene	6 M KOH	-1.15 V	-84.5	25 min, 50 CV	[156]
Fe-Ni-Graphene	6 M KOH	-1.18 V	-88.1	25 min, 50 CV	[157]
Mo_2C/Graphene	0.5 M H_2SO_4	8 mV	58	20 h, 3000 CV	[158]
Ni_2P-Graphene@NF	1 M KOH	7 mV	30	15 h, 500 CV	[159]
$NiMo_2C$@C	1 M KOH	65 mV	84	10 h, 2000 CV	[160]
N-doped Mesoporous Graphene	0.5 M H_2SO_4	340 mV	109	5000 CV	[161]
Pd/Graphene	0.5 M H_2SO_4	~100 mV	46	1000 CV	[162]
MoS_2/GO	0.5 M H_2SO_4	-107 mV	86.3	2000 CV	[163]
Cu_2ZnSnS_4/GO	0.5 M H_2SO_4	53.1 mV	70	1000 CV	[164]
Rh-GO	0.5 M H_2SO_4	2 mV	10	7000 s	[165]
MoS_x/GO	0.5 M H_2SO_4	195 mV	47.7	500 CV, 10,000 s	[166]
GO@Ni	1 M H_2SO_4	83.2 mV	55.7	30 h	[167]
$Ni_{0.85}Se$/N-GO	0.5 M H_2SO_4	104 mV	50.7	20 h	[168]
Pt/GO/Ni-Cu/NF	1 M KOH	31 mV	51	6000 s, 1000 CV	[169]
FeS_2/GO	0.5 M H_2SO_4	250 mV	64	-	[170]
FeS_2/rGO	0.5 M H_2SO_4	139 mV	66	500 min, 1000 CV	[171]
W-Mo-O/rGO	0.1 M $HClO_4$	50 mV	46	2000 CV	[172]
CoP-rGO	0.5 M H_2SO_4	-	104.8	500 CV	[173]
NiS_2/rGO	0.5 M H_2SO_4	200 mV	52	3000 CV	[174]
Co-Ni-P/rGO	1 M KOH	207 mV	65	30 h	[175]
Au-Pd/rGO	0.5 M H_2SO_4	-0.8 mV	29	24 h, 5000 CV	[176]
MoP/rGO	0.5 M H_2SO_4	82 mV	42	20 h	[177]
P-MoS_2/N,S-rGO	0.5 M H_2SO_4	94 mV	47	-	[178]
CoP/rGO	1 M KOH	36.6 mV	43.1	20 h, 5000 CV	[179]

11. Photo-Electrocatalytic H_2 Production

The photoelectrochemical (PEC) water-splitting pathway propounds an ultimate route for the production of H_2 energy using solar light and electricity [180]. The ideal catalyst for PEC H_2 generation should have some essential features, such as cost-effectiveness, ample abundance, a non-toxic nature, narrow band edge, effective surface area, intrinsic conductivity, long-term stability and high mobility for charge carriers [181–184]. Figure 18 demonstrates the necessary requirements for an appropriate semiconducting material as a photo-electrode for water splitting. Photo-electrocatalysis imitates the natural photosynthesis Z-scheme in which photo-induced electrons and holes transfer to the cathode and anode surface to take part in the water reduction and oxidation reaction, respectively. As the reaction sites are spatially segregated, that eliminates the need to separate H_2 and O_2. The PEC system conventionally requires a minimum of two electrodes (cathode and anode) to propel the reduction and oxidation reactions independently [185]. In a conventional PEC system, p-type and n-type semiconductors are anchored as a photo-cathode and photo-anode, respectively. The Gibbs free energy required for a water-splitting reaction to ensue is +237 KJ mol^{-1}, which is equal to -1.23 eV for H_2 evolution [186]. Consequently, at least 1.23 eV band energy is obligatory and ought to be supplied from solar light sources [187,188]. For water oxidation and reduction processes, the thermodynamic potentials are 1.23 eV and 0 eV, respectively [187,189,190]. For effective PEC and photocatalytic operations, the band locations of the targeted catalyst should be appropriate for water oxidation and reduction; thus, the location of the conduction band should be below 0 eV, and the location of the valence band should be higher than 1.23 eV [191,192].
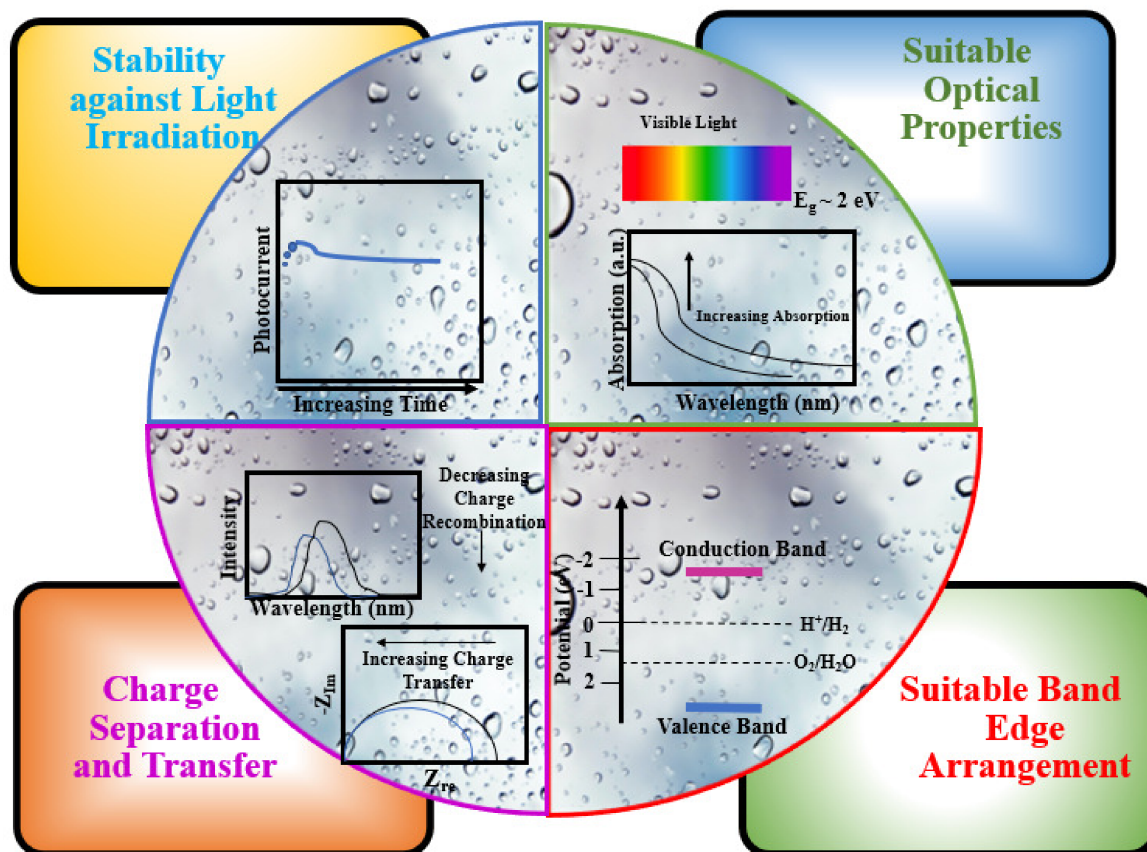
Figure 18. Important requirements for an appropriate semiconducting material as a photoelectrode for water splitting process.

Graphene-based heterostructures are scrutinized as the most propitious catalysts due to the excellent electrical conductivity of graphene and its derivatives. The band gap of primary catalysts can be tuned by the appropriate doping of graphene-based derivatives, as these compounds exhibit versatile electronic properties. At the time of PEC operation, when the catalytic system is irradiated, the photo-generation of the charge carriers takes place at the semiconducting base, where graphene-based derivatives participate in the process of charge transfer. The major part of the graphene in the binary/ternary heterostructures is to serve as a transporter, electron acceptor and mediator, having a 2D conductive structure [193–200]. Graphene, owing to its unique layered structure, accelerates the electron–hole segregation and transport of electrons in distinct photo-electrodes. The application, fabrication and design of graphene-based catalysts in photo-electrodes for H_2 evolution through PEC water-splitting have emerged as promising in research areas.

12. Graphene/GO/rGO as Photo-Electrocatalysts

For the ideal photo-electrode, the catalytic system should have features such as a befitting band gap, ample sunlight absorption, suitable alignments of the band energy levels, advanced stability, excellent charge transport properties and environmental benignity. To attain all of these benchmarks, materials such as graphene, GO and rGO displayed tremendous potential for solar-propelled H_2 generation via PEC water splitting. Nevertheless, these substances have shown marvelous response toward PEC to a certain limit; however, they also have experienced many drawbacks in practical utilizations. These materials experienced low light absorption due to their thin 2D structure; as a consequence, they need to be combined with other semiconductor catalysts for efficient H_2 generation. Samsudin et al. [201] prepared $BiVO_4$/Graphene quantum dots (GQD)/g-C_3N_4 to

examine and compare their PEC H_2 generation performance with binaryBiVO$_4$/g-C$_3$N$_4$ heterostructures. The BiVO$_4$/GQD/g-C$_3$N$_4$ achieved a photocurrent density as high as 19.2 mA cm^{-2}, which had an effectively improved performance by 75.7% as compared to its binary counterpart. The enhanced results stemmed from the graphene quantum dots, which served as an outstanding electron transporter within the system of the ternary heterostructure. Cheng et al. [202] synthesized Au and TiO$_2$ quantum dots on 3D graphene flowers (Au@TiO$_2$@3DGFs) for PEC H$_2$ production through water splitting. The as-synthesized composite demonstrated an astonishing PEC result by achieving a 90 mA cm^{-2} photocurrent density with stunning chemical stability. The improved results were attributed to the synergistic effect between 3DGFs and TiO$_2$ by not only attaining a high surface area but also by accelerating the segregation of the photo-generated charge carriers. MoS$_2$/N- doped graphene nanocomposites were prepared by Carraro et al. [203] to investigate the PEC activity for H$_2$ production. The MoS$_2$/N-doped graphene nanocomposites exhibited seven-fold better results in comparison to the bare MoS$_2$.The enhanced outcomes were attributed to the nanojunction formed between MoS$_2$ and N-doped grapheme, which promoted effective electron–hole pair separation. Garcia et al. [204] prepared N-doped graphene as photoelectrodes for H$_2$ generation. The N-doped graphene showed constant H$_2$ evolution with a 60 mA cm^{-2} photocurrent density. Yuan et al. [205] fabricated Polyaniline/Graphene Oxide/TiO$_2$ (PANI-GO-TiO$_2$) ternary hybrids to examine the PEC H$_2$ evolution activity. The results of the as-prepared ternary hybrids showed a greater H$_2$ evolution rate than most of the TiO$_2$-based nanocatalysts reported. Figure 19a illustrates that the synergistic effect between GO and PANI efficiently improved the segregation efficiency of photo-excited charge carriers, thus, enhancing the PEC performance. The best photocurrent observed was 0.13 mA cm^{-2}, as shown in Figure 19b, which was attributed to the combined effect of GO/TiO$_2$ and PANI. Figure 19c demonstrates the band structure, and the mechanism of charge transfer of PANI/GO/TiO$_2$ ternary hybrid films.

In another work, a PbS-Graphene Oxide-Polyaniline nanocomposite was fabricated by Shaban et al. [206] to study its PEC activity for H$_2$ production. The catalytic efficiency of the as-engineered heterostructure was enhanced as the optimum photocurrent density was found to be 1.75 mA cm^{-2}. Gupta et al. [207] synthesized Bi$_2$Ti$_2$O$_7$/reduced graphene oxide (BTO/rGO) to examine and compare the PEC H$_2$ production activity with BTO alone. The outcome illustrated the enhanced current response of the BTO/rGO composite that was 41 μA than the BTO photocurrent (2.8 μA). The upgraded results were indeed credited to the addition of rGO, which facilitated the removal and transportation of electrons that inhibited the recombination of the charge carriers. Zhao et al. [208] fabricated g-C$_3$N$_4$-rGO on Ni foam (CNG/Ni) for H$_2$ generation through PEC water splitting. The as-prepared CNG1.0/Ni showed the highest photocurrent density, as depicted in Figure 20a. The maximum PEC activity of CNG/Ni observed was around 6.0 μmolh^{-1}cm^{-2}, with remarkable durability, as revealed in Figure 20b,c. The effective H$_2$ evolution results stemmed from the interface formation between rGO and g-C$_3$N$_4$, which effectively enhanced the generation of photo-excited electron–hole pairs and suppressed the recombination rate of the charge carriers, as demonstrated in Figure 20d.

A study has been reported in which Aykuz et al. [209] prepared N/B/P-doped rGO-Cd$_{0.60}$Zn$_{0.40}$S heterostructures to test the PEC activity for H$_2$ generation. Figure 21a demonstrates the scheme of the photocatalytic hydrogen evolution reaction (PCHER) and photo-electrocatalytic hydrogen evolution reaction (PECHER). The N-doped rGO/Cd$_{0.60}$Zn$_{0.4}$0S displayed the best results among the fabricated heterostructures. The conduction and valence band potentials of the N-doped rGO/Cd$_{0.60}$Zn$_{0.40}$S were −0.46 V and 1.97 V, respectively, calculated from the photo-voltages observed in Figure 21b. The photocurrent density of N-doped rGO/Cd$_{0.60}$Zn$_{0.40}$S was obtained to be 0.92 mA cm^{-2}, as shown in Figure 21c, which was ascribed to the efficient segregation and transfer of the charge carriers.
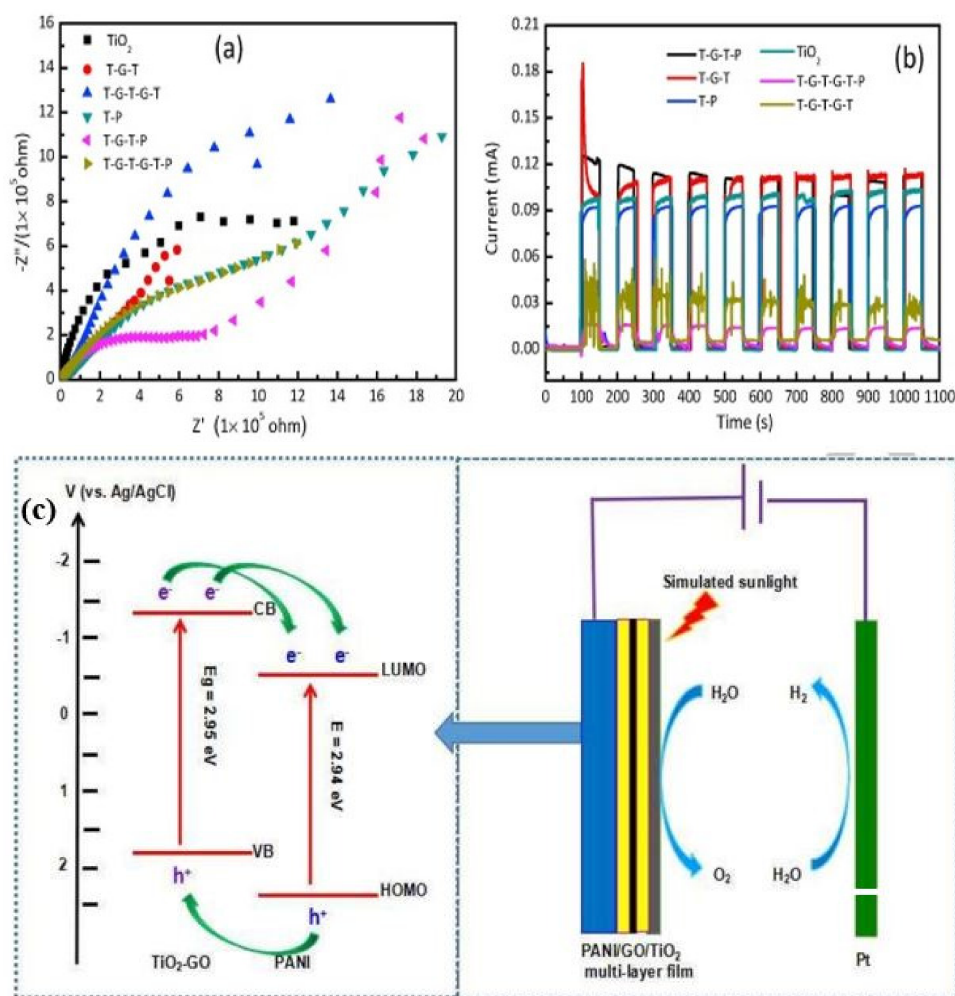
Figure 19. (**a**) EIS spectra of TiO_2, GO/TiO_2, $PANI/TiO_2$ and $PANI/GO/TiO_2$ hybrid films electrodes. The frequency range of 100 kHz-0.01 Hz, an amplitude of 10 mV at an applied potential of +0.6 V, the electrolyte was of 0.42 mol L^{-1} NaCl, 0.055 mol L^{-1} $MgCl_2$ and 0.029 mol L^{-1} Na_2SO_4. (**b**) The photocurrent response of hybrid film electrodes. The potential of the working electrode was set as 0.6 V vs. Ag/AgCl/3M KCl. (**c**) Sketching map of energy band structure, charge separation and PEC hydrogen generation mechanism for ternary $PANI/GO/TiO_2$ film electrode. (Reprinted with permission from reference [205]. Copyright 2018, Elsevier).

Samsudin et al. [210] embedded rGO on g-$C_3N_4/BiVO_4$ for $PECH_2$ generation. The g-$C_3N_4/BiVO_4$ demonstrated a 9.73 mA cm^{-2} photocurrent density, which was the result of resistivity in the migration of the photo-induced charge carriers, while the incorporation of rGO on g-$C_3N_4/BiVO_4$ immensely improved the photocurrent density (14.44 mA cm^{-2}) by inhibiting the recombination rate of the photo-excited charge carriers. Mo-TiO_2/rGO nanocomposites were designed by Dargahi et al. [211] to examine the PEC performance for H_2 evolution. The as-prepared optimized heterostructure showed boosted PEC activity as the photocurrent density was achieved to be 55.8 μA cm^{-2}, which was nearly eight-fold higher than pristine TiO_2. The tailoring of the band gap from 3.12 eV of pristine TiO_2 to 2.22 eV of the Mo-TiO_2/rGO. The improved PEC performance stemmed from the depletion of the band gap and the effective segregation and increased time span of the recombination of the electron–hole pairs. Rambabu et al. [212] fabricated a TiO_2/rGO/CdS ternary catalyst system that showed a high photocurrent density of ~11 mA cm^{-2}. The improved results were attributed to the charge segregation property of rGO. In another work, GO/rGO layers were deposited on TiO_2 nanotubes by Rambabu et al. [213] and compared the PEC activity for the water splitting of pristine TiO_2, rGO/TiO_2 and GO/TiO_2. The rGO-deposited TiO_2

nanotubes showed an enhanced photocurrent because of the higher charge transfer and separation rate of the photo-induced electrons from TiO_2, having a low-resistance path provided by rGO. Long et al. [214] fabricated $ZnAgInSe/TiO_2/GO$ photoelectrode for hydrogen generation. The photocurrent density of the as-fabricated photoelectrode was found to be ~6.7 mA cm^{-2}, which attributed to the synergistic effect between ZnAgInSe QDs and TiO_2/GO.
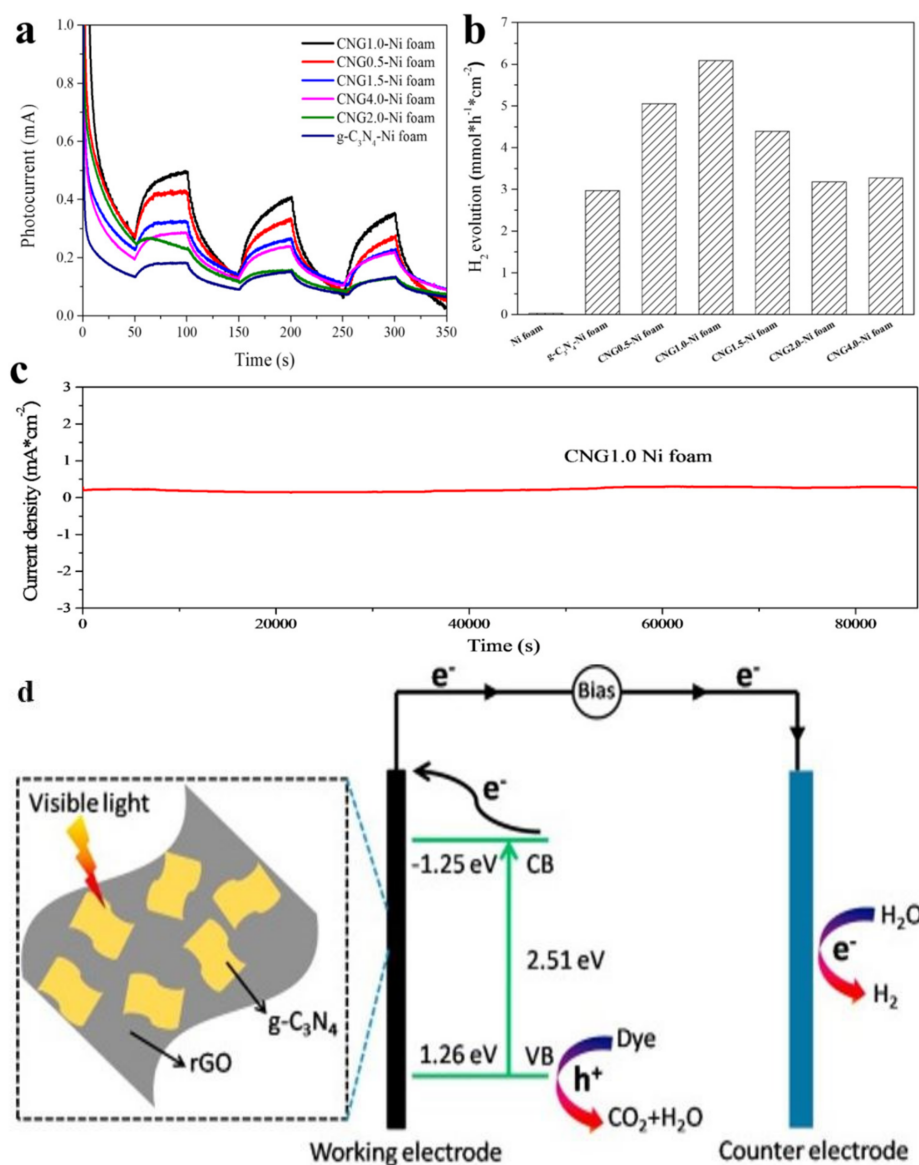

Figure 20. (**a**) Photocurrent responses of CNG1.0-Ni foam electrode and g-C_3N_4-Ni foam electrode under visible-light (λ > 420 nm) irradiation. (**b**) H_2 evolution rates of pure Ni electrode, g-C_3N_4-Ni foam electrode and CNG-Ni foam electrode with different percentages of rGO. (**c**) Current density of CNG1.0-Ni foam electrode within 24 h. (**d**) Schematic depiction showing the energy diagram and electron migration process of CNG1.0-Ni foam electrode. (Reprinted with permission from reference [208]. Copyright 2019, Elsevier).

Carbon element graphene and its derivatives hold magnificent potential as functional nanomaterials owing to their outstanding conductivity, relatively higher surface area and cost-effectiveness. However, as far as PEC water splitting is concerned, there are still some challenges to meet for graphene and its derivatives, such as graphene having no or zero electronic band gap, it must be hybridized with other photo-active substances for PEC applications. On the grounds of some excellent results mentioned above, it is

crystal clear that they have further paved the way for graphene and its derivatives for their employment as photo-electrodes in PEC applications. On that account, systemized and organized studies are compulsory to deduce the nature of the junction formed between graphene/GO/rGO and semiconductors, which are still lacking for PEC water splitting. The catalytic efficiency of a few graphene derivative-based heterostructured PEC catalysts is demonstrated in Table 5.
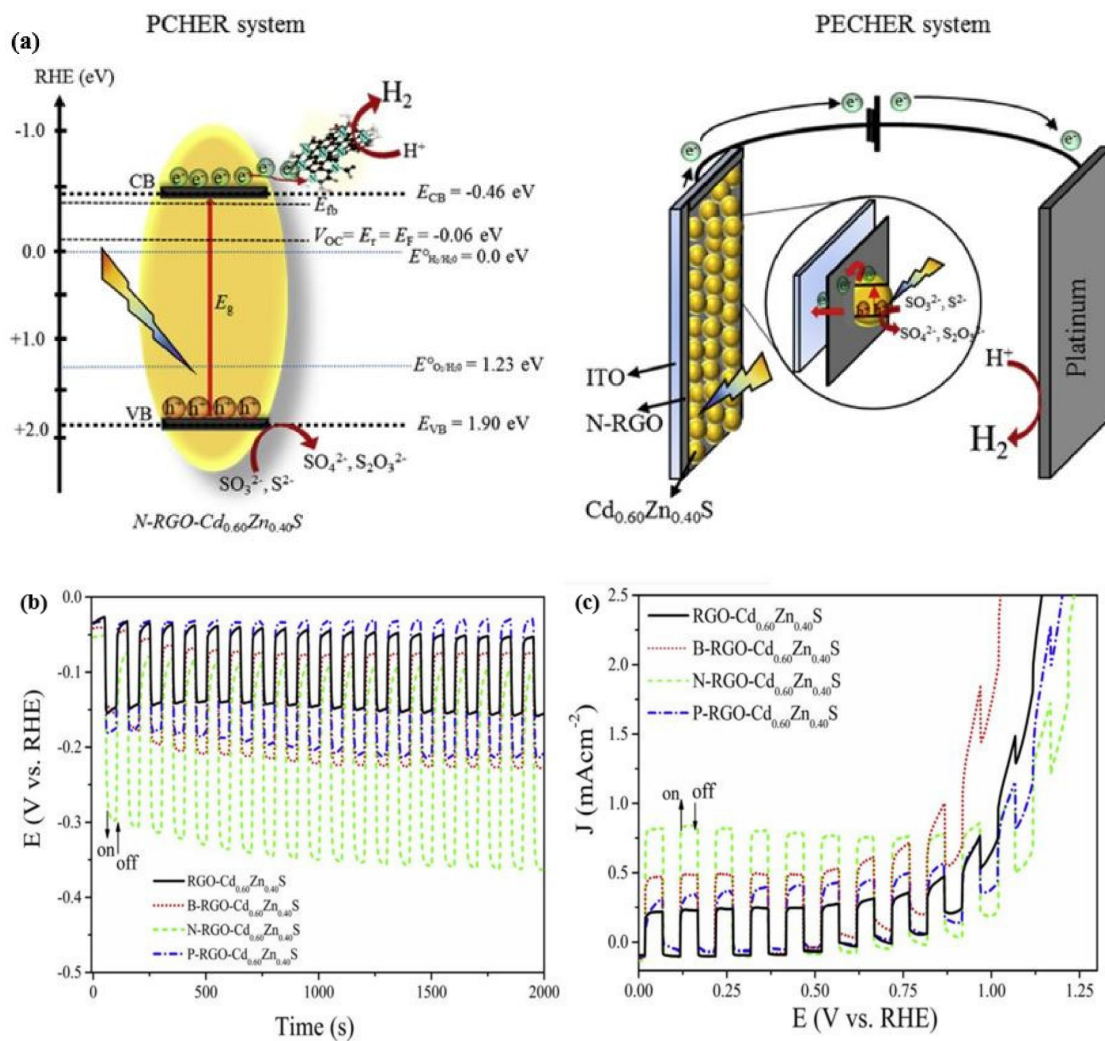

Figure 21. (**a**) Schematic illustration for PCHER and PECHER systems. (**b**) Open-circuit potential (OCP) versus time under on/off of visible light irradiation with interval 50 s. (**c**) The linear sweep voltammograms of the photocatalysts under visible light irradiation. (Reprinted with permission from reference [209]. Copyright 2019, Elsevier).

Table 5. Summary of PEC activity by graphene and its derivative photoelectrodes.

Photo-Electrocatalyst	Electrolyte	Light Source/ Photoconversion Efficiency	Band Gap	Photocurrent Density	Ref.
$BiVO_4$/GQD/g-C_3N_4	0.5 Na_2SO_4	500 W Halogen Lamp/0.57%	2.47 eV	19.2 mA cm^{-2}	[201]
Au/TiO_2/3DGFs	1 M KOH	Xenon Lamp	-	90 mA cm^{-2}	[202]
MoS_2/N-Graphene	0.5 M H_2SO_4	White LED Lamp	~1.7 eV	94 mA cm^{-2}	[203]
PANI-GO-TiO_2	NaCl, $MgCl_2$, Na_2SO_4	300 W Xenon Lamp	2.50 eV	0.13 mA cm^{-2}	[205]
PbS-Graphene Oxide-PANI	0.3 M $Na_2S_2O_3$	400 W Metal Halide Lamp/1.75%	1.16, 2.0 eV	1.75 mA cm^{-2}	[206]
BTO/rGO	0.5 M NaOH	500 W Xenon Lamp	2.26 eV	41 μA	[207]

Table 5. *Cont.*

Photo-Electrocatalyst	Electrolyte	Light Source/ Photoconversion Efficiency	Band Gap	Photocurrent Density	Ref.
CNG/Ni	Methanol, 0.5 M NaOH	300 W Xenon Lamp	2.51 eV	1.0 mA cm^{-2}	[208]
N-doped rGO-Cd$_{0.60}$Zn$_{0.40}$S	Na$_2$S/Na$_2$SO$_3$	300 W Xenon Lamp/1.77%	2.43 eV	0.92 mA cm^{-2}	[209]
rGO/g-C$_3$N$_4$/BiVO$_4$	0.5 M Na$_2$SO$_4$	500 W Halogen Lamp/0.41%	2.54 eV	14.44 mA cm^{-2}	[210]
Mo-TiO$_2$/rGO	0.1 M Na$_2$SO$_4$	PHILIPS PL-S9W lamp	2.22 eV	55.8 µA cm^{-2}	[211]
TiO$_2$/rGO/CdS	Na$_2$S/Na$_2$SO$_3$	Xenon Lamp/5.11%	~2.2 eV	~11 mA cm^{-2}	[212]
rGO/TiO$_2$	0.5 M Na$_2$SO$_4$	300 W Xenon Lamp/0.12%	-	0.26 mA/cm^2	[213]
ZnAgInSe/TiO$_2$/GO	Na$_2$S/Na$_2$SO$_3$	AM 1.5G, 100 mW/cm^2	~1.82 eV	~6.7 mA/cm^2	[214]

13. Conclusions

In this review, we have summarized the latest effective research on the designing and utilization of graphene and its derivative-based photocatalysts for photochemical H$_2$ evolution. The incorporation of graphene and its derivatives in these photocatalysts improved the photochemical performance impressively, possessing an extended range for light absorption, a higher surface area and magnificent electron conductivity. The encouraging quantum leap of cost-effective graphene and GO/rGO-based electrocatalysts has been concluded as the substitute to costly nanomaterials toward efficient HER. Different electrocatalysts with synergistic effects between graphene and its derivative have been meticulously reviewed. In general, possessing a large surface area, excellent chemical stability and high electrical conductivity, graphene and GO/rGO-based electrocatalysts have been broadly studied by researchers, and huge inspiring attainments have been developed in recent years. It has been concluded that graphene and its derivatives have enormous capability as utilitarian nanomaterials for PEC water splitting. Mainly, they have received attention due to their enhanced charge transport kinetics, having loftier electrical conductivity. However, there is limited research in the area of PEC water splitting containing graphene/GO/rGO-based photo-electrodes. There is still much scope available to exploit them as photo-electrodes to understand their features in a much better way for PEC water splitting. In order to have scalable applicability of graphene-based derivative catalytic systems toward H$_2$ evolution via photochemical, electrochemical and photoelectrochemical water splitting pathways, it is fundamental to optimize the operational conditions, such as the robustness, longevity and stability of graphene-based derivative catalytic systems, homogeneity in the light-harvesting and voltage applied during an experimental run and most importantly their adaptability and superiority over conventional energy sources.

14. Perspectives and Outlook

Since the last century, the dependency on fossil derivative fuels for meeting energy demands has escalated dramatically; as a consequence, at present, approximately 80 percent of the energy requirement is served by fossil derivative fuels globally. As of now, everybody is heavily paying for price-utilizing excessive fossil fuel for energy production, which has exacted a colossal toll on the environment and humanity. The effects of the utilization of these conventional energy sources are dreadful as ice sheets and glaciers are dwindling, lakes and rivers are scattering before their geological time, geographic ranges of animals and plants are repositioning and the habitat of flora and fauna is perturbed. Realizing all of these consequences, it is high time for the energy transition towards sustainable sources and end the fossil fuel domain once and for all. Green H$_2$ fuel is glorified as the fuel of the future, and of course, as a remedy to the energy crisis and air pollution. However, it is fundamental to produce it without any harmful emissions; otherwise, it would no longer be considered a green H$_2$ fuel. Overall, water splitting provides such a propitious strategy for the production of H$_2$ that generates no or zero harmful emissions. Water splitting includes PWS, EWS and PEC water splitting, which have received significant attention but still, H$_2$ production via water splitting is somehow expensive, which is why it is lacking behind its

far-reaching applications. The need for cost-effective catalysts is in high demand; therefore, graphene and its derivatives, such as graphene-oxide and reduced graphene-oxide, have come into enlightenment as a substitute for precious noble metal catalysts.

15. Advancements in Photocatalytic Hydrogen Evolution

Some benchmark improvements have been obtained via graphene derivative-based PWS for efficient H_2 energy. Nevertheless, there is always a scope for further improvement, and it is needed in this emerging field to achieve optimally effective graphene and its derivative-based photocatalysts. As an example, a stronger understanding of the mechanisms of photochemical performance improvement by graphene and its derivatives is still a challenge but is pivotal for fabricating novel and superior graphene and its derivative-based photocatalysts. To shed light on the mechanism of the photochemical process, all features in the relationship of fabrication, property and structure will have to be understood better. Further research is still required to build more advanced heterostructures, specifically binary and ternary graphene-based heterostructures. In the binary or ternary heterostructures, band-gap tuning of the constituent substances can ease the charge segregation effectively at a distinct level. Additionally, the developments of highly effective methodologies are desired for the extensive interfacial relationships between graphene derivatives and primary photocatalysts to enhance the photochemical activity. The above-mentioned results of graphene or GO, rGO-based derivatives illustrated that electrical conductivity played a key role in the interfacial connection between graphene or GO, rGO and photocatalyst in understanding the photochemical H_2 evolution. Hence, more effective fabrication strategies for graphene and its derivative-based photocatalysts would be in demand to address these matters.

16. Advancements in Electrocatalytic Hydrogen Evolution

With the excessive achievements of electrocatalytic HER in recent years, the addition of graphene and its derivatives have been acknowledged as beneficial to enhancing performance and increasing durability. Despite continuous developments in graphene and the GO- and rGO-based electrocatalysts that have been accomplished, even now, there are some challenges that demand attention to resolve for far-reaching applications. The actual catalytic performance of the active control center in the structure of graphene and its derivatives is cloudy. While an HER takes place, a complex reconstruction on the structure usually occurs on the surface of the catalyst, which hugely modifies the environment of the control center and chemical structure, creating a difficult situation to understand the catalytic mechanism. For that reason, there is a need for advanced characterization techniques to untangle the structural progress of the active control center and provide improvised guidelines for the design of catalysts. As graphene and its derivatives can be synthesized via diverse routes, there are clear differences appear in physiochemical features in the resulting products. During the stage of study and application, the utilization of distinct types of graphene and its derivatives creates hurdles in the quality of the HER. This condition implies the urgency of establishing and ensuring a unified approach to measuring the features of graphene and its derivatives, which maintains the continuous enhancements in graphene and its derivative-based electrocatalytic HER.

17. Advancements in Photo-Electrocatalytic Hydrogen Evolution

However, despite the fact that graphene and its derivatives have a number of merits for PEC water splitting, there is still too little research reported that corresponds to PEC water splitting. This issue needs further systematic exploration of how the interfacial features dominate the photo-conversion mechanism and how the synthesis should be carried out for the most effective graphene and its derivatives containing heterostructures with superior PEC performance for water splitting. The study of the interface between the photoactive components and graphene and its derivatives at molecular levels should be carried out using a mechanistic approach to better achieve HER results. On that account,

more attempts should be made toward controlling, modifying and understanding the catalytic performance of graphene and its derivatives.

References

1. Rezazadeh, A.A.; Avami, A.; Mashayekhi, M.; Kianbakhsh, A. Assessing the contribution of different sources in atmospheric dispersion of PM2.5 and related health impact in a region of Qazvin, Iran. *Air Qual. Atmos. Health* **2022**, *15*, 1379–1394. [CrossRef]
2. Pietrosemoli, L.; Monroy, C.R. The Venezuelan energy crisis: Renewable energies in the transition towards sustainability. *Renew. Sustain. Energy Rev.* **2019**, *105*, 415–426. [CrossRef]
3. Ali, S.A.; Ahmad, T. Chemical strategies in molybdenum based chalcogenides nanostructures for photocatalysis. *Int. J. Hydrog. Energy* **2022**, *47*, 29255–29283. [CrossRef]
4. Ibrahim, R.L. Beyond COP26: Can income level moderate fossil fuels, carbon emissions, and human capital for healthy life expectancy in Africa? *Environ. Sci. Pollut. Res.* **2022**, *29*, 87568–87582. [CrossRef]
5. Hassan, A.; Ilyas, S.Z.; Jalil, A.; Ullah, Z. Monetization of the environmental damage caused by fossil fuels. *Environ. Sci. Pollut. Res.* **2021**, *28*, 21204–21211. [CrossRef]
6. IEA, Oil Demand Forecast, 2010–2026, Prepandemic and in Oil 2021, IEA, Paris. Available online: https://www.iea.org/data-and-statistics/charts/oil-demand-forecast-2010-2026-pre-pandemic-and-in-oil-2021. (accessed on 30 September 2020).
7. IEA, Global Energy Review 2021, IEA, Paris. Available online: https://www.iea.org/reports/global-energy-review-2021 (accessed on 30 April 2021).
8. Ulucak, R. How do environmental technologies affect green growth? Evidence from BRICS economies. *Sci. Total Environ.* **2020**, *712*, 136504.
9. Smirnova, E.; Kot, S.; Kolpak, E.; Shestak, V. Governmental support and renewable energy production: A cross-country review. *Energy* **2021**, *230*, 120903. [CrossRef]
10. Muneer, T.; Asif, M. Energy supply, its demand and security issues for developed and emerging economies. *Renew. Sustain. Energy Rev.* **2007**, *11*, 1388–1413.
11. Roy, B.; Schaffartzik, A. Talk renewables, walk coal: The paradox of India's energy transition. *Ecol. Econ.* **2021**, *180*, 106871. [CrossRef]
12. Zheng, H.; Song, M.; Shen, Z. The evolution of renewable energy and its impact on carbon reduction in China. *Energy* **2021**, *237*, 121639. [CrossRef]
13. IEA, Change in Energy Demand and Renewables Output in Electricity, Heat and Transport, 2019 to 2020, IEA, Paris. Available online: https://www.iea.org/data-and-statistics/charts/change-in-energy-demand-and-renewables-output-in-electricity-heat-and-transport-2019-to-2020 (accessed on 30 November 2020).
14. Mehtab, A.; Ahmed, J.; Alshehri, S.M.; Mao, Y.; Ahmad, T. Rare earth doped metal oxide nanoparticles for photocatalysis: A perspective. *Nanotechnology* **2022**, *33*, 142001. [CrossRef]
15. Yu, Z.Y.; Duan, Y.; Feng, X.Y.; Yu, X.; Gao, M.R.; Yu, S.H. Clean and affordable hydrogen fuel from alkaline water splitting: Past, recent progress, and future prospects. *Adv. Mater.* **2021**, *33*, 2007100. [CrossRef]
16. Mehtab, A.; Alshehri, S.M.; Ahmad, T. Photocatalytic and photoelectrocatalytic water splitting by porous g-C3N4 nanosheets for hydrogen generation. *Acs Appl. Nano Mater.* **2022**, *5*, 12656–12665. [CrossRef]
17. Turner, J.A. Sustainable Hydrogen Production. *Science* **2004**, *305*, 972–974. [CrossRef]

18. Chu, S.; Majumdar, A. Opportunities and challenges for a sustainable energy future. *Nature* **2012**, *488*, 294–303. [CrossRef]
19. Xia, Z. Hydrogen evolution: Guiding principles. *Nat. Energy* **2016**, *1*, 1–2. [CrossRef]
20. Hosseini, S.E.; Wahid, M.A. Hydrogen production from renewable and sustainable energy resources: Promising green energy carrier for clean development. *Renew. Sustain. Energy Rev.* **2016**, *57*, 850–866. [CrossRef]
21. Staffell, I.; Scamman, D.; Abad, A.V.; Balcombe, P.; Dodds, P.E.; Ekins, P.; Shah, N.; Ward, K.R. The role of hydrogen and fuel cells in the global energy system. *Energy Environ. Sci.* **2019**, *12*, 463–491. [CrossRef]
22. Winter, C.J. Hydrogen energy Abundant, efficient, clean: A debate over the energy-system-of-change. *Int. J. Hydrog. Energy* **2009**, *34*, S1–S52. [CrossRef]
23. Larminie, J.; Dicks, A.; McDonald, M.S. *Fuel Cell Systems Explained*; J. Wiley: Chichester, UK, 2003; Volume 2, pp. 207–225.
24. Momirlan, M.; Veziroglu, T.N. The properties of hydrogen as fuel tomorrow in sustainable energy system for a cleaner planet. *Int. J. Hydrog. Energy* **2005**, *30*, 795–802. [CrossRef]
25. Hosseini, S.E.; Wahid, M.A. Hydrogen from solar energy, a clean energy carrier from a sustainable source of Energy. *Int. J. Energy Res.* **2020**, *44*, 4110–4131. [CrossRef]
26. Veziroglu, T.N. Conversion to hydrogen economy. *Energy Procedia* **2012**, *29*, 654–656. [CrossRef]
27. Iordache, I.; Gheorghe, A.V.; Iordache, M. Towards a hydrogen economy in Romania: Statistics, technical and scientific general aspects. *Int. J. Hydrog. Energy* **2013**, *38*, 12231–12240. [CrossRef]
28. Prabhukhot, P.R.; Wagh, M.M.; Gangal, A.C. A review on solid state hydrogen storage material. *Adv. Energy Power* **2016**, *4*, 11–22.
29. Sahaym, U.; Norton, M.G. Advances in the application of nanotechnology in enabling a 'Hydrogen economy'. *J. Mater. Sci.* **2008**, *43*, 5395–5429. [CrossRef]
30. Bossel, U.; Eliasson, B. Energy and the Hydrogen Economy. 2003. Available online: https://afdc.energy.gov/files/pdfs/hyd_economy_bossel_eliasson.pdf (accessed on 30 November 2020).
31. Edwards, P.P.; Kuznetsov, V.L.; David, W.I. Hydrogen Energy. *Philos. Trans. R. Soc. A.* **2007**, *365*, 1043–1056.
32. Niaz, S.; Manzoor, T.; Pandith, A.H. Hydrogen storage: Materials, methods and perspectives. *Renew. Sustain. Energy Rev.* **2015**, *50*, 457–469. [CrossRef]
33. Rosen, M.A.; Koohi-Fayegh, S. The prospects for hydrogen as an energy carrier: An overview of hydrogen energy and hydrogen energy systems. *Energy Ecol. Environ.* **2016**, *1*, 10–29. [CrossRef]
34. Bockris, J.O.M. The hydrogen economy: Its history. *Int. J. Hydrog. Energy* **2013**, *38*, 2579–2588. [CrossRef]
35. Scheer, R.; Nielson, T.; Glickson, D. *Hydrogen Storage "Think Tank"*; Department of Energy, Office of Hydrogen, Fuel Cells and Infrastructure Technologies: Washington, DC, USA, 2003.
36. IEA, The Future of Hydrogen, IEA, Paris. Available online: https://www.iea.org/reports/the-future-of-hydrogen (accessed on 30 June 2019).
37. IEA, Energy Technology Perspectives 2020, IEA, Paris. Available online: https://www.iea.org/reports/energy-technology-perspectives-2020 (accessed on 30 September 2020).
38. Schlesinger, H.I.; Brown, H.C.; Finholt, A.E.; Gilbreath, J.R.; Hoekstra, H.R.; Hyde, E.K. Sodium borohydride, its hydrolysis and its use as a reducing agent and in the generation of hydrogen 1. *J. Am. Chem. Soc.* **1953**, *75*, 215–219. [CrossRef]
39. Abdelhamid, H.N. A review on hydrogen generation from the hydrolysis of sodium borohydride. *Int. J. Hydrog. Energy* **2021**, *46*, 726–765. [CrossRef]
40. Naimi, Y.; Antar, A. Hydrogen generation by water electrolysis. In *Advances in Hydrogen Generation Technologies*; Intech: London, UK, 2018; Volume 1.
41. Mehtab, A.; Banerjee, S.; Mao, Y.; Ahmad, T. Type-II CuFe2O4/Graphitic-Carbon Nitride heterojunctions for high efficiency photocatalytic and electrocatalytic hydrogen generation. *Acs Appl. Mater. Interfaces* **2022**, *14*, 44317–44329. [CrossRef] [PubMed]
42. Voziuk, O.; Tanchoux, N.; Millet, J.M.M.; Albonetti, S.; Renzo, F.D.; Cavani, F. Spinel mixed oxides for chemical-loop reforming: From solid state to potential application. *Stud. Surf. Sci. Catal.* **2019**, *178*, 281–302.
43. Maeda, K.; Domen, K. Photocatalytic water splitting: Recent progress and future challenges. *J. Phys. Chem. Lett.* **2010**, *1*, 2655–2661. [CrossRef]
44. Farooq, U.; Ahmed, J.; Alshehri, S.M.; Mao, Y.; Ahmad, T. Self-Assembled interwoven nanohierarchitectures of NaNbO3 and NaNb1−xTaxO3 (0.05 ≤ x ≤ 0. 20): Synthesis, structural characterization, photocatalytic applications, and dielectric properties. *Acs Omega* **2022**, *7*, 16952–16967. [CrossRef]
45. Ahmad, H.; Kamarudin, S.K.; Minggu, L.J.; Kassim, M. Hydrogen from photo-catalytic water splitting process: A review. *Renew. Sustain. Energy Rev.* **2015**, *43*, 599–610. [CrossRef]
46. Ahmad, T.; Farooq, U.; Phul, R. Fabrication and photocatalytic applications of perovskite Materials with special emphasis on alkali-metal-based niobates and tantalates. *Ind. Eng. Chem. Res.* **2018**, *57*, 18–41. [CrossRef]
47. Jang, J.; Kim, H.; Lee, J.S. Heterojunction semiconductors: A strategy to develop efficient photocatalytic materials for visible light water splitting. *Catal. Today.* **2012**, *185*, 270–277. [CrossRef]
48. Khan, H.; Lone, I.H.; Lofland, S.E.; Ramanujachary, K.V.; Ahmad, T. Exploiting Multiferroicity of TbFeO3 Nanoparticles for Hydrogen Generation through Photo/Electro/Photoelectro-catalytic Water Splitting. *Int. J. Hydrog. Energy* **2022**. [CrossRef]
49. Lalitha, K.; Reddy, J.K.; Sharma, M.V.P.; Kumari, V.D.; Subrahmanyam, M. Continuous hydrogen production activity over finely dispersed Ag2O/TiO2 catalysts from methanol: Water mixtures under solar irradiation: A structure–activity correlation. *Int. J. Hydrog. Energy* **2010**, *35*, 3991–4001. [CrossRef]

50. Huang, B.; Chang, F.; Wey, M. Photocatalytic properties of redox-treated Pt/TiO2 photocatalysts for H2 production from an aqueous methanol solution. *Int. J. Hydrog. Energy* **2010**, *35*, 7699–7705. [CrossRef]

51. Nguyen, V.N.H.; Amal, R.; Beydoun, D. Effect of formate and methanol on photoreduction/removal of toxic cadmium ions using TiO$_2$ semiconductor as photocatalyst. *Chem. Eng. Sci.* **2003**, *58*, 4429–4439. [CrossRef]

52. Farooq, U.; Phul, R.; Alshehri, S.M.; Ahmed, J.; Ahmad, T. Electrocatalytic and enhanced photocatalytic applications of sodium niobate nanoparticles developed by citrate precursor route. *Sci. Rep.* **2019**, *9*, 1–17. [CrossRef]

53. Alshehri, S.M.; Ahmed, J.; Ahamad, T.; Alhokbany, N.; Arunachalam, P.; Al-Mayouf, A.M.; Ahmad, T. Synthesis, characterization, multifunctional electrochemical (OGR/ORR/SCs) and photodegradable activities of ZnWO4 nanobricks. *J. Solgel Sci. Technol.* **2018**, *87*, 137–146. [CrossRef]

54. Ahmed, J.; Ahamad, T.; Alhokbany, N.; Almaswari, B.M.; Ahmad, T.; Hussain, A.; Al-Farraj, E.S.S.; Alshehri, S.M. Molten salts derived copper tungstate nanoparticles as bifunctional electro-catalysts for electrolysis of water and supercapacitor applications. *Chemelectrochem* **2018**, *5*, 3938–3945. [CrossRef]

55. Wang, S.; Lu, A.; Zhong, C. Hydrogen production from water electrolysis: Role of catalysts. *Nano Converg.* **2021**, *8*, 1–23. [CrossRef]

56. Ding, C.; Shi, J.; Wang, Z.; Li, C. Photoelectrocatalytic water splitting: Significance of cocatalysts, electrolyte, and interfaces. *Acs Catal.* **2017**, *7*, 675–688. [CrossRef]

57. Naaz, F.; Sharma, A.; Shahazad, M.; Ahmad, T. Hydrothermally Derived Hierarchical CuO Nanoflowers as an Efficient Photocatalyst and Electrocatalyst for Hydrogen Evolution. *ChemistrySelect* **2022**, *7*, e202201800. [CrossRef]

58. Alekseeva, O.K.; Pushkareva, I.V.; Pushkarev, A.S.; Fateev, V.N. Graphene and Graphene-Like Materials for Hydrogen Energy. *Nanotechnol. Russ.* **2020**, *15*, 273–300. [CrossRef]

59. Xiang, Q.; Yu, J. Graphene-based photocatalysts for hydrogen generation. *J. Phys. Chem. Lett.* **2013**, *4*, 753–759. [CrossRef]

60. Tareen, A.K.; Khan, K.; Iqbal, M.; Zhang, Y.; Long, J.; Nazeer, F.; Mahmood, A.; Mahmood, N.; Shi, Z.; Ma, C.; et al. Recent advances in novel graphene: New horizons in renewable energy storage technologies. *J. Mater. Chem. C* **2022**, *10*, 11472–11531. [CrossRef]

61. Marcano, D.C.; Kosynkin, D.V.; Berlin, J.M.; Sinitskii, A.; Sun, Z.; Slesarev, A.; Alemany, L.B.; Lu, W.; Tour, J.M. Improved synthesis of graphene oxide. *Acs Nano* **2010**, *4*, 4806–4814. [CrossRef] [PubMed]

62. Torres, T. Graphene chemistry. *Chem. Soc. Rev.* **2017**, *46*, 4385–4386. [CrossRef] [PubMed]

63. Dasari, B.L.; Nouri, J.M.; Brabazon, D.; Naher, S. Graphene and derivatives–Synthesis techniques, properties and their energy applications. *Energy* **2017**, *140*, 766–778. [CrossRef]

64. Shah, M.A.; Ahmad, T. *Nano Science & Technology*; I.K. International Pvt. Ltd.: New Delhi, India, 2021.

65. Zhang, L.H.; Shi, Y.; Wang, Y.; Shiju, N.R. Nanocarbon catalysts: Recent understanding regarding the active sites. *Adv. Sci.* **2020**, *7*, 1902126. [CrossRef]

66. Jain, S.K.; Farooq, U.; Jamal, F.; Kalam, A.; Ahmad, T. Hydrothermal assisted synthesis and structural characterization of Zn doped SnO2 nanoparticles for catalytic reduction of 4-nitrophenol. *Mater. Today Proc.* **2021**, *36*, 717–723. [CrossRef]

67. Naaz, F.; Shamsi, A.; Jain, S.K.; Kalam, A.; Ahmad, T. Tin Oxide Nanocatalyst Assisted Transformation of p-Nitrophenol to p-Aminophenol. *Mater. Today Proc.* **2021**, *36*, 708–716. [CrossRef]

68. Song, Y.; Zou, W.; Lu, Q.; Lin, L.; Liu, Z. Graphene transfer: Paving the road for applications of chemical vapor deposition graphene. *Small* **2021**, *17*, 2007600. [CrossRef]

69. Ahmad, T.; Ganguli, A.K. Structural and dielectric characterization of nanocrystalline (Ba,Pb)ZrO3 developed by reverse micellar synthesis. *J. Am. Ceram. Soc.* **2006**, *89*, 3140–3146. [CrossRef]

70. Ahmad, T.; Ganguli, A.K. Reverse micellar route to nanocrystalline titanates (SrTiO3, Sr2TiO4, and PbTiO3): Structural aspects and dielectric properties. *J. Am. Ceram. Soc.* **2006**, *89*, 1326–1332. [CrossRef]

71. Ahmad, T.; Lone, I.H.; Ubaidullah, M. Structural characterization and multiferroic properties of hexagonal nanosized YMnO3 developed by a low temperature precursor route. *Rsc Adv.* **2015**, *5*, 58065–58071. [CrossRef]

72. Ubaidullah, M.; Lone, I.H.; Al-Hartomy, O.A.; Kumar, D.; Ahmad, T. Metal Organic Precursor Route for Pb-Substituted BaZrO3 Nanoceramics: Structural Characterization and Properties. *Adv. Sci. Lett.* **2014**, *20*, 1354–1359. [CrossRef]

73. Diab, K.R.; El-Maghrabi, H.H.; Nada, A.A.; Youssef, A.M.; Hamdy, A.; Roualdes, S.; El-Wahab, S.A. Facile fabrication of NiTiO$_3$/graphene nanocomposites for photocatalytic hydrogen generation. *J. Photochem. Photobiol. A Chem.* **2018**, *365*, 86–93. [CrossRef]

74. Du, C.; Ao, Q.; Cao, N.; Yang, L.; Luo, W.; Chang, G. Facile synthesis of monodisperse ruthenium nanoparticles supported on graphene for hydrogen generation from hydrolysis of ammonia borane. *Int. J. Hydrog. Energy* **2015**, *40*, 6180–6187. [CrossRef]

75. Aksoy, B.T.; Çoşut, B. Graphene/graphene oxide–based nanomaterials for hydrogen production and storage applications. In *Nanomaterials for Hydrogen Storage Applications*; Elsevier: Amsterdam, The Netherlands, 2021; pp. 97–116.

76. Liu, G.; Jin, W.; Xu, N. Two-dimensional-material membranes: A new family of high-performance separation membranes. Angew. *Chem. Int. Ed. Engl.* **2016**, *55*, 13384–13397. [CrossRef]

77. Lin, L.C.; Grossman, J.C. Atomistic understandings of reduced graphene oxide as an ultrathin-film nanoporous membrane for separations. *Nat. Commun.* **2015**, *6*, 1–7. [CrossRef]

78. Chen, D.; Feng, H.; Li, J. Graphene oxide: Preparation, functionalization, and electrochemical applications. *Chem. Rev.* **2012**, *112*, 6027–6053. [CrossRef]

79. Wang, M.; Ju, P.; Li, J.; Zhao, Y.; Han, X.; Hao, Z. Facile synthesis of MoS2/g-C3N4/GO ternary heterojunction with enhanced photocatalytic activity for water splitting. *Acs Sustain. Chem. Eng.* **2017**, *5*, 7878–7886. [CrossRef]

80. Khan, Z.; Chetia, T.R.; Vardhaman, A.K.; Barpuzari, D.; Sastri, C.V.; Qureshi, M. Visible light assisted photocatalytic hydrogen generation and organic dye degradation by CdS–metal oxide hybrids in presence of graphene oxide. *Rsc Adv.* **2012**, *2*, 12122–12128. [CrossRef]

81. Yap, P.L.; Kabiri, S.; Auyoong, Y.L.; Tran, D.N.; Losic, D. Tuning the multifunctional surface chemistry of reduced graphene oxide via combined elemental doping and chemical modifications. *Acs Omega* **2019**, *4*, 19787–19798. [CrossRef]

82. Shahdeo, D.; Roberts, A.; Abbineni, N.; Gandhi, S. Graphene based sensors. *Compr. Anal. Chem.* **2020**, *91*, 175–199.

83. Zhang, C.; Lv, W.; Zhang, W.; Zheng, X.; Wu, M.B.; Wei, W.; Tao, Y.; Li, Z.; Yang, Q.H. Reduction of graphene oxide by hydrogen sulfide: A promising strategy for pollutant control and as an electrode for Li-S batteries. *Adv. Energy Mater.* **2014**, *4*, 1301565. [CrossRef]

84. Park, S.; An, J.; Potts, J.R.; Velamakanni, A.; Murali, S.; Ruoff, R.S. Hydrazine-reduction of graphite- and graphene oxide. *Carbon* **2011**, *49*, 3019–3023. [CrossRef]

85. Si, Y.; Samulski, E.T. Synthesis of water soluble graphene. *Nano Lett.* **2008**, *8*, 1679–1682. [CrossRef]

86. Stankovich, S.; Dikin, D.A.; Dommett, G.H.; Kohlhaas, K.M.; Zimney, E.J.; Stach, E.A.; Piner, R.D.; Nguyen, S.T.; Ruoff, R.S. Graphene-based composite materials. *Nature* **2006**, *442*, 282–286. [CrossRef]

87. Stankovich, S.; Dikin, D.A.; Piner, R.D.; Kohlhaas, K.A.; Kleinhammes, A.; Jia, Y.; Wu, Y.; Nguyen, S.T.; Ruoff, R.S. Synthesis of graphene-based nanosheets via chemical reduction of exfoliated graphite oxide. *Carbon* **2007**, *45*, 1558–1565. [CrossRef]

88. Wang, G.; Yang, J.; Park, J.; Wang, B.; Liu, H.; Yao, J. Facile synthesis and characterization of graphene nanosheets. *J. Phys. Chem. C* **2008**, *112*, 8192–8195. [CrossRef]

89. Shin, H.J.; Kim, K.K.; Benayad, A.; Yoon, S.M.; Park, H.K.; Jung, I.S.; Jin, M.H.; Jeong, H.K.; Kim, J.M.; Choi, J.Y.; et al. Efficient reduction of graphite oxide by sodium borohydride and its effect on electrical conductance. *Adv. Funct. Mater.* **2009**, *19*, 1987–1992. [CrossRef]

90. Park, S.; Park, G.D.; Ko, D.; Kang, Y.C.; Piao, Y. Aerosol synthesis of molybdenum diselenide–reduced graphene oxide composite with empty nanovoids and enhanced hydrogen evolution reaction performances. *Chem. Eng. J.* **2017**, *315*, 355–363. [CrossRef]

91. Ha, E.; Liu, W.; Wang, L.; Man, H.; Hu, L.; Tsang, S.C.E.; Chan, C.T.; Kwok, W.; Lee, L.Y.S.; Wong, K. Cu2ZnSnS4/MoS2-reduced graphene oxide heterostructure: Nanoscale interfacial contact and enhanced photocatalytic hydrogen generation. *Sci. Rep.* **2017**, *7*, 1–8. [CrossRef]

92. Jain, S.K.; Pandit, N.A.; Fazil, M.; Ali, S.A.; Ahmed, J.; Alshehri, S.M.; Mao, Y.; Ahmad, T. Chemical fabrication, structural characterization and photocatalytic water splitting application of Sr-doped SnO2 nanoparticles. *Nanotechnology* **2022**, *33*, 355706. [CrossRef]

93. Xiang, Q.J.; Yu, J.G.; Jaroniec, M. Graphene-based semiconductor photocatalysts. *Chem. Soc. Rev.* **2012**, *41*, 782–796. [CrossRef]

94. Jain, S.K.; Fazil, M.; Pandit, N.A.; Ali, S.A.; Naaz, F.; Khan, H.; Mehtab, A.; Ahmed, J.; Ahmad, T. Modified, Solvothermally Derived Cr-doped SnO2 nanostructures for enhanced photocatalytic and electrochemical water-splitting applications. *Acs Omega* **2022**, *7*, 14138–14147. [CrossRef]

95. Farooq, U.; Naz, F.; Phul, R.; Pandit, N.A.; Jain, S.K.; Ahmad, T. Development of heterostructured ferroelectric SrZrO3/CdS photocatalysts with enhanced surface area and photocatalytic activity. *J. Nanosci. Nanotechnol.* **2020**, *20*, 3770–3779. [CrossRef]

96. Liu, S.W.; Yu, J.G.; Cheng, B.; Jaroniec, M. Fluorinated semiconductor photocatalysts: Tunable synthesis and unique properties. *Adv. Colloid Interface Sci.* **2012**, *173*, 35–53. [CrossRef]

97. Jain, S.K.; Fazil, M.; Naaz, F.; Pandit, N.A.; Ahmed, J.; Alshehri, S.M.; Mao, Y.; Ahmad, T. Silver-doped SnO2 nanostructures for photocatalytic water splitting and catalytic nitrophenol reduction. *New J. Chem.* **2022**, *46*, 2846–2857. [CrossRef]

98. Liu, S.W.; Yu, J.G.; Jaroniec, M. Anatase TiO2 with dominant high-energy {001} facets: Synthesis, properties, and applications. *Chem. Mater.* **2011**, *23*, 4085–4093. [CrossRef]

99. Ahmad, T.; Phul, R.; Alam, P.; Lone, I.H.; Shahazad, M.; Ahmed, J.; Ahamad, T.; Alshehri, S.M. Dielectric, optical and enhanced photocatalytic properties of CuCrO2 nanoparticles. *Rsc Adv.* **2017**, *7*, 27549–27557. [CrossRef]

100. An, X.Q.; Yu, J.C. Graphene-based photocatalytic composites. *Rsc Adv.* **2011**, *1*, 1426–1434. [CrossRef]

101. Lin, X.; Du, S.; Li, C.; Li, G.; Li, Y.; Chen, F.; Fang, P. Consciously constructing the robust NiS/g-C3N4 hybrids for enhanced photocatalytic hydrogen evolution. *Catal. Lett.* **2020**, *150*, 1898–1908. [CrossRef]

102. Chen, P.; Liu, F.; Ding, H.; Chen, S.; Chen, L.; Li, Y.J.; Au, C.T.; Yin, S.F. Porous double-shell CdS@C3N4 octahedron derived by in situ supramolecular self-assembly for enhanced photocatalytic activity. *Appl. Catal. B Environ.* **2019**, *252*, 33–40. [CrossRef]

103. Tang, N.; Li, Y.; Chen, F.; Han, Z. In situ fabrication of a direct Z-scheme photocatalyst by immobilizing CdS quantum dots in the channels of graphene-hybridized and supported mesoporous titanium nanocrystals for high photocatalytic performance under visible light. *Rsc Adv.* **2018**, *8*, 42233–42245. [CrossRef] [PubMed]

104. Zhang, N.; Zhang, Y.H.; Xu, Y.J. Recent progress on graphene-based photocatalysts: Current status and future perspectives. *Nanoscale* **2012**, *4*, 5792–5813. [CrossRef] [PubMed]

105. Han, L.; Wang, P.; Dong, S.J. Progress in Graphene-based photoactive nanocomposites as a promising class of photocatalyst. *Nanoscale* **2012**, *4*, 5814–5825. [CrossRef] [PubMed]

106. Kamat, P.V. Graphene-based nanoassemblies for energy conversion. *J. Phys. Chem. Lett.* **2011**, *2*, 242–251. [CrossRef]

107. Li, X.; Yu, J.; Wageh, S.; Al-Ghamdi, A.A.; Xie, J. Graphene in photocatalysis: A review. *Small* **2016**, *12*, 6640–6696. [CrossRef]

108. Suresh, R.; Mangalaraja, R.V.; Mansilla, H.D.; Santander, P.; Yáñez, J. Reduced graphene oxide-based photocatalysis. In *Green Photocatalysts*; Springer: Berlin, Germany, 2020; pp. 145–166.

109. Tiwari, S.; Kumar, S.; Ganguli, A.K. Role of MoS2/rGO co-catalyst to enhance the activity and stability of Cu2O as photocatalyst towards photoelectrochemical water splitting. *J. Photochem. Photobiol. A: Chem.* **2022**, *424*, 113622. [CrossRef]

110. Lin, J.; Pan, H.; Chen, Z.; Wang, L.; Li, Y.; Zhu, S. Graphene-based nanomaterials for solar-driven overall water splitting. *Chem. Eur. J.* **2022**, *28*, e202200722.

111. Farooq, U.; Chaudhary, P.; Ingole, P.P.; Kalam, A.; Ahmad, T. Development of cuboidal KNbO3@ α-Fe2O3 hybrid nanostructures for improved photocatalytic and photoelectrocatalytic applications. *Acs Omega* **2020**, *5*, 20491–20505. [CrossRef]

112. Yu, R.; Yang, Y.; Zhou, Z.; Li, X.; Gao, J.; Wang, N.; Li, J.; Liu, Y. Facile synthesis of ternary heterojunction Bi2O2/reduced graphene oxide/TiO2 composite with boosted visible-light photocatalytic activity. *Sep. Purif. Technol.* **2022**, *299*, 121712. [CrossRef]

113. Xiang, Q.J.; Yu, J.G.; Jaroniec, M. Preparation and enhanced visible-light photocatalytic H2-production activity of graphene/C3N4composites. *J. Phys. Chem. C* **2011**, *115*, 7355–7363. [CrossRef]

114. Leary, R.; Westwood, A. Carbonaceous Nanomaterials for the Enhancement of TiO2 Photocatalysis. *Carbon* **2011**, *49*, 741–772. [CrossRef]

115. Kamat, P.V. Graphene-based nanoarchitectures. Anchoring semiconductor and metal nanoparticles on a two-dimensional carbon support. *J. Phys. Chem. Lett.* **2010**, *1*, 520–527. [CrossRef]

116. Khalid, N.R.; Ahmed, E.; Ahmad, M.; Niaz, N.A.; Ramzan, M.; Shakil, M.; Iqbal, T.; Majid, A. Microwave-assisted synthesis of Ag–TiO2/graphene composite for hydrogen production under visible light irradiation. *Ceram. Int.* **2016**, *42*, 18257–18263. [CrossRef]

117. Xia, Y.; Cheng, B.; Fan, J.; Yu, J.; Liu, G. Unraveling photoexcited charge transfer pathway and process of CdS/graphene nanoribbon composites toward visible-light photocatalytic hydrogen evolution. *Small* **2019**, *15*, 1902459. [CrossRef]

118. Yu, X.; Du, R.; Li, B.; Zhang, Y.; Liu, H.; Qu, J.; An, X. Biomolecule-assisted self-assembly of CdS/MoS2/graphene hollow spheres as high-efficiency photocatalysts for hydrogen evolution without noble metals. *Appl. Catal. B Environ.* **2016**, *182*, 504–512. [CrossRef]

119. Yue, Z.; Liu, A.; Zhang, C.; Huang, J.; Zhu, M.; Du, Y.; Yang, P. Noble-metal-free hetero-structural CdS/Nb2O5/N-doped-graphene ternary photocatalytic system as visible-light-driven photocatalyst for hydrogen evolution. *Appl. Catal. B Environ.* **2017**, *201*, 202–210. [CrossRef]

120. Khalid, N.R.; Liaqat, M.; Tahir, M.B.; Nabi, G.; Iqbal, T.; Niaz, N.A. The role of graphene and europium on TiO2 performance for photocatalytic hydrogen evolution. *Ceram. Int.* **2018**, *44*, 546–549. [CrossRef]

121. Chang, C.J.; Chu, K.W.; Hsu, M.H.; Chen, C.Y. Ni-doped ZnS decorated graphene composites with enhanced photocatalytic hydrogen-production performance. *Int. J. Hydrog. Energy* **2015**, *40*, 14498–14506. [CrossRef]

122. Xiang, Q.; Cheng, F.; Lang, D. Hierarchical layered WS2/graphene-modified CdS nanorods for efficient photocatalytic hydrogen evolution. *Chemsuschem* **2016**, *9*, 996–1002. [CrossRef]

123. Chang, C.J.; Lin, Y.G.; Weng, H.T.; Wei, Y.H. Photocatalytic hydrogen production from glycerol solution at room temperature by ZnO-ZnS/graphene photocatalysts. *Appl. Surf. Sci.* **2018**, *451*, 198–206. [CrossRef]

124. Raghavan, A.; Sarkar, S.; Nagappagari, L.R.; Bojja, S.; Muthukonda, V.S.; Ghosh, S. Decoration of graphene quantum dots on TiO2 nanostructures: Photosensitizer and cocatalyst role for enhanced hydrogen generation. *Ind. Eng. Chem. Res.* **2020**, *59*, 13060–13068. [CrossRef]

125. Yeh, T.F.; Syu, J.M.; Cheng, C.; Chang, T.H.; Teng, H. Graphite oxide as a photocatalyst for hydrogen production from water. *Adv. Funct. Mater.* **2010**, *20*, 2255–2262. [CrossRef]

126. Gao, P.; Liu, J.; Lee, S.; Zhang, T.; Sun, D.D. High quality graphene oxide–CdS–Pt nanocomposites for efficient photocatalytic hydrogen evolution. *J. Mater. Chem.* **2012**, *22*, 2292–2298. [CrossRef]

127. Rahman, M.Z.; Zhang, J.; Tang, Y.; Davey, K.; Qiao, S.Z. Graphene oxide coupled carbon nitride homo-heterojunction photocatalyst for enhanced hydrogen production. *Mater. Chem. Front.* **2017**, *1*, 562–571. [CrossRef]

128. Gliniak, J.; Lin, J.H.; Chen, Y.T.; Li, C.R.; Jokar, E.; Chang, C.H.; Peng, C.S.; Lin, J.N.; Lien, W.H.; Tsai, H.M.; et al. Sulfur-doped graphene oxide quantum dots as photocatalysts for hydrogen generation in the aqueous phase. *ChemSusChem* **2017**, *10*, 3260–3267. [CrossRef]

129. Zhou, Y.; Zhang, L.; Qin, L.; Kang, S.Z.; Li, X. A mixed phase lanthanum vanadate in situ induced by graphene oxide/graphite carbon nitride for efficient photocatalytic hydrogen generation. *Int. J. Hydrog. Energy* **2021**, *46*, 27495–27505. [CrossRef]

130. Tie, L.; Liu, Y.; Shen, S.; Yu, C.; Mao, C.; Sun, J.; Sun, J. In-situ construction of graphene oxide in microsphere ZnS photocatalyst for high-performance photochemical hydrogen generation. *Int. J. Hydrog. Energy* **2020**, *45*, 16606–16613. [CrossRef]

131. Pei, F.; Liu, Y.; Xu, S.; Lü, J.; Wang, C.; Cao, S. Nanocomposite of graphene oxide with nitrogen-doped TiO2 exhibiting enhanced photocatalytic efficiency for hydrogen evolution. *Int. J. Hydrog. Energy* **2013**, *38*, 2670–2677. [CrossRef]

132. Gao, X.; Wang, J.; Xue, Q.; Ma, Y.Y.; Gao, Y. AgBr/polyoxometalate/graphene oxide ternary composites for visible light-driven photocatalytic hydrogen production. *Acs Appl. Nano Mater.* **2021**, *4*, 2126–2135. [CrossRef]

133. Wang, G.; Wang, F.; Liu, S.; Li, M.; Xie, M.; Yang, Z.; Xiang, Y.; Lv, S.; Han, W. Construction of heterojuncted photocatalyst with TiO2 quantum dots and graphene oxide nanosheets for highly efficient photocatalysis. *Scr. Mater.* **2021**, *199*, 113862. [CrossRef]

134. Peng, T.; Li, K.; Zeng, P.; Zhang, Q.; Zhang, X. Enhanced photocatalytic hydrogen production over graphene oxide–cadmium sulfide nanocomposite under visible light irradiation. *J. Phys. Chem. C* **2012**, *116*, 22720–22726. [CrossRef]

135. Gultom, N.S.; Abdullah, H.; Kuo, D.H. Effects of graphene oxide and sacrificial reagent for highly efficient hydrogen production with the costless Zn(O,S) photocatalyst. *Int. J. Hydrog. Energy* **2019**, *44*, 29516–29528. [CrossRef]

136. Wang, P.; Zhan, S.; Xia, Y.; Ma, S.; Zhou, Q.; Li, Y. The fundamental role and mechanism of reduced graphene oxide in rGO/Pt-TiO$_2$ nanocomposite for high-performance photocatalytic water splitting. *Appl. Catal. B Environ.* **2017**, *207*, 335–346. [CrossRef]

137. Wang, X.; Yao, X. Photocatalytic hydrogen generation of ZnO rod–CdS/reduced graphene oxide heterostructure prepared by Pt-induced oxidation and light irradiation-assisted methods. *Carbon* **2014**, *77*, 667–674. [CrossRef]

138. Tran, P.D.; Batabyal, S.K.; Pramana, S.S.; Barber, J.; Wong, L.H.; Loo, S.C.J. A cuprous oxide–reduced graphene oxide (Cu$_2$O–rGO) composite photocatalyst for hydrogen generation: Employing rGO as an electron acceptor to enhance the photocatalytic activity and stability of Cu$_2$O. *Nanoscale* **2012**, *4*, 3875–3878. [CrossRef]

139. Shaheer, A.M.; Vinesh, V.; Lakhera, S.K.; Neppolian, B. Reduced graphene oxide as a solid-state mediator in TiO$_2$/In$_{0.5}$WO$_3$ S-scheme photocatalyst for hydrogen production. *Sol. Energy* **2021**, *213*, 260–270. [CrossRef]

140. Yadav, A.A.; Hunge, Y.M.; Kang, S.W. Spongy ball-like copper oxide nanostructure modified by reduced graphene oxide for enhanced photocatalytic hydrogen production. *Mater. Res. Bull.* **2021**, *133*, 111026. [CrossRef]

141. He, G.L.; Zhong, Y.H.; Chen, M.J.; Li, X.; Fang, Y.P.; Xu, Y.H. One-pot hydrothermal synthesis of SrTiO$_3$-reduced graphene oxide composites with enhanced photocatalytic activity for Hydrogen production. *J. Mol. Catal. A Chem.* **2016**, *423*, 70–76. [CrossRef]

142. Xue, W.; Hu, X.; Liu, E.; Fan, J. Novel reduced graphene oxide-supported Cd0.5Zn0.5S/g-C3N4 Z-scheme heterojunction photocatalyst for enhanced hydrogen evolution. *Appl. Surf. Sci.* **2018**, *447*, 783–794. [CrossRef]

143. Ye, L.; Fu, J.; Xu, Z.; Yuan, R.; Li, Z. Facile one-pot solvothermal method to synthesize sheet-on-sheet reduced graphene oxide (RGO)/ZnIn$_2$S$_4$ nanocompositeswith superior photocatalytic performance. *Acs Appl. Mater. Interfaces* **2014**, *6*, 3483–3490. [CrossRef] [PubMed]

144. Hafeez, H.Y.; Lakhera, S.K.; Bellamkonda, S.; Rao, G.R.; Shankar, M.V.; Bahnemann, D.W.; Neppolian, B. Construction of ternary hybrid layered reduced graphene oxide supported g-C$_3$N$_4$-TiO$_2$ nanocomposite and its photocatalytic hydrogen production activity. *Int. J. Hydrog. Energy* **2018**, *43*, 3892–3904. [CrossRef]

145. Zeng, P.; Zhang, Q.; Peng, T.; Zhang, X. One-pot synthesis of reduced graphene oxide–cadmium sulfide nanocomposite and its photocatalytic hydrogen production. *Phys. Chem. Chem. Phys.* **2011**, *13*, 21496–21502. [CrossRef] [PubMed]

146. Jiao, Y.; Zheng, Y.; Jaroniec, M.; Qiao, S.Z. Design of Electrocatalysts for Oxygen- and Hydrogen-Involving Energy Conversion Reactions. *Chem. Soc. Rev.* **2015**, *44*, 2060–2086. [CrossRef] [PubMed]

147. You, B.; Sun, Y. Chalcogenide and Phosphide Solid-State Catalysts for H2 Generation. *ChemPlusChem* **2016**, *81*, 1045–1055. [CrossRef]

148. Zhu, Y.P.; Guo, C.; Zheng, Y.; Qiao, S.Z. Surface and interface engineering of noble-metal-free electrocatalysts for efficient energy conversion processes. *Acc. Chem. Res.* **2017**, *50*, 915–923. [CrossRef]

149. Pandit, B.; Rondiya, S.R.; Shaikh, S.F.; Ubaidullah, M.; Amaral, R.; Dzade, N.Y.; Goda, E.S.; Rana, A.H.S.; Gill, H.S.; Ahmad, T. Regulated electrochemical performance of manganese oxide cathode for potassium-ion batteries: A combined experimental and first-principles density functional theory (DFT) investigation. *J. Colloid Interface Sci.* **2022**, *633*, 886–896. [CrossRef]

150. Bae, S.Y.; Jeon, I.Y.; Mahmood, J.; Baek, J.B. Molybdenum-based carbon hybrid materials to enhance the hydrogen evolution reaction. *Chem. Eur. J.* **2018**, *24*, 18158–18179. [CrossRef]

151. Liu, X.; Jiao, Y.; Zheng, Y.; Davey, K.; Qiao, S.Z. A computational study on Pt and Ru dimers supported on graphene for the hydrogen evolution reaction: New insight into the alkaline mechanism. *J. Mater. Chem. A* **2019**, *7*, 3648–3654. [CrossRef]

152. Zhou, W.; Jia, J.; Lu, J.; Yang, L.; Hou, D.; Li, G.; Chen, S. Recent developments of carbon-based electrocatalysts for hydrogen evolution reaction. *Nano Energy* **2016**, *28*, 29–43. [CrossRef]

153. Zhang, G.; Wang, G.; Liu, Y.; Liu, H.; Qu, J.; Li, J. Highly active and stable catalysts of phytic acid-derivative transition metal phosphides for full water splitting. *J. Am. Chem. Soc.* **2016**, *138*, 14686–14693. [CrossRef]

154. Xu, X.; Liang, H.; Ming, F.; Qi, Z.; Xie, Y.; Wang, Z. Prussian blue analogues derived penroseite (Ni,Co)Se$_2$ nanocages anchored on 3D graphene aerogel for efficient water splitting. *Acs Catal.* **2017**, *7*, 6394–6399. [CrossRef]

155. Fei, H.; Dong, J.; Arellano-Jiménez, M.J.; Ye, G.; Kim, N.D.; Samuel, E.L.; Peng, Z.; Zhu, Z.; Qin, F.; Bao, J.; et al. Atomic cobalt on nitrogen-doped graphene for hydrogen generation. *Nat. Commun.* **2015**, *6*, 1–8. [CrossRef]

156. Subramanya, B.; Ullal, Y.; Shenoy, S.U.; Bhat, D.K.; Hegde, A.C. Novel Co–Ni–graphene composite electrodes for hydrogen production. *Rsc Adv.* **2015**, *5*, 47398–47407. [CrossRef]

157. Badrayyana, S.; Bhat, D.K.; Shenoy, S.; Ullal, Y.; Hegde, A.C. Novel Fe–Ni-Graphene composite electrode for hydrogen production. *Int. J. Hydrog. Energy* **2015**, *40*, 10453–10462. [CrossRef]

158. Huo, L.; Liu, B.; Zhang, G.; Zhang, J. Universal strategy to fabricate a two-dimensional layered mesoporous Mo$_2$C electrocatalyst hybridized on graphene sheets with high activity and dura-bility for hydrogen generation. *Acs Appl. Mater. Interfaces* **2016**, *8*, 18107–18118. [CrossRef]

159. Han, A.; Jin, S.; Chen, H.; Ji, H.; Sun, Z.; Du, P. A robust hydrogen evolution catalyst based on crystalline nickel phosphide nanoflakes on three-dimensional graphene/nickel foam: High performance for electrocatalytic hydrogen production from pH 0–14. *J. Mater. Chem. A* **2015**, *3*, 1941–1946. [CrossRef]

160. Li, X.; Yang, L.; Su, T.; Wang, X.; Sun, C.; Su, Z. Graphene-coated hybrid electrocatalysts derived from bimetallic metal–organic frameworks for efficient hydrogen generation. *J. Mater. Chem. A.* **2017**, *5*, 5000–5006. [CrossRef]

161. Huang, X.; Zhao, Y.; Ao, Z.; Wang, G. Micelle-template synthesis of nitrogen-doped mesoporous graphene as an efficient metal-free electrocatalyst for hydrogen production. *Sci. Rep.* **2014**, *4*, 1–6. [CrossRef]

162. Ghasemi, S.; Hosseini, S.R.; Nabipour, S.; Asen, P. Palladium nanoparticles supported on graphene as an efficient electrocatalyst for hydrogen evolution reaction. *Int. J. Hydrog. Energy* **2015**, *40*, 16184–16191. [CrossRef]

163. Zhou, W.; Zhou, K.; Hou, D.; Liu, X.; Li, G.; Sang, Y.; Liu, H.; Li, L.; Chen, S. Three-dimensional hierarchical frameworks based on MoS2 nanosheets self-assembled on graphene oxide for efficient electrocatalytic hydrogen evolution. *Acs Appl. Mater. Interfaces* **2014**, *6*, 21534–21540. [CrossRef] [PubMed]

164. Digraskar, R.V.; Sapner, V.S.; Mali, S.M.; Narwade, S.S.; Ghule, A.V.; Sathe, B.R. CZTS deco-rated on graphene oxide as an efficient electrocatalyst for high-performance hydrogen evolution reaction. *Acs Omega* **2019**, *4*, 7650–7657. [CrossRef] [PubMed]

165. Narwade, S.S.; Mali, S.M.; Sapner, V.S.; Sathe, B.R. Graphene oxide decorated with Rh nanospheres for electrocatalytic water splitting. *Acs Appl. Nano Mater.* **2020**, *3*, 12288–12296. [CrossRef]

166. Hu, W.H.; Shang, X.; Han, G.Q.; Dong, B.; Liu, Y.R.; Li, X.; Chai, Y.M.; Liu, Y.Q.; Liu, C.G. MoSx supported graphene oxides with different degree of oxidation as efficient electrocatalysts for hydrogen evolution. *Carbon* **2016**, *100*, 236–242. [CrossRef]

167. Sarawutanukul, S.; Phattharasupakun, N.; Sawangphruk, M. 3D CVD graphene oxide-coated Ni foam as carbo-and electro-catalyst towards hydrogen evolution reaction in acidic solution: In situ electrochemical gas chromatography. *Carbon* **2019**, *151*, 109–119. [CrossRef]

168. Fu, H.; Chen, Y.; Ren, Z.; Xiao, Y.; Liu, Y.; Zhang, X.; Tian, G. Highly dispersed of Ni0.85Se nanoparticles on nitrogen-doped graphene oxide as efficient and durable electrocatalyst for hydrogen evolution reaction. *Electrochim. Acta.* **2018**, *262*, 107–114. [CrossRef]

169. Lotfi, N.; Shahrabi, T.; Yaghoubinezhad, Y.; Darband, G.B. Direct electrodeposition of platinum nanoparticles@ graphene oxide@ nickel-copper@ nickel foam electrode as a durable and cost-effective catalyst with remarkable performance for electrochemical hydrogen evolution reaction. *Appl. Surf. Sci.* **2020**, *505*, 144571. [CrossRef]

170. Theerthagiri, J.; Sudha, R.; Premnath, K.; Arunachalam, P.; Madhavan, J.; Al-Mayouf, A.M. Growth of iron diselenide nanorods on graphene oxide nanosheets as advanced electrocatalyst for hydrogen evolution reaction. *Int. J. Hydrog. Energy* **2017**, *42*, 13020–13030. [CrossRef]

171. Chen, Y.; Xu, S.; Li, Y.; Jacob, R.J.; Kuang, Y.; Liu, B.; Wang, Y.; Pastel, G.; Salamanca-Riba, L.G.; Zachariah, M.R.; et al. FeS2 nanoparticles embedded in reduced graphene oxide toward robust, high-performance electrocatalysts. *Adv. Energy Mater.* **2017**, *7*, 1700482. [CrossRef]

172. Imran, M.; Yousaf, A.B.; Zaidi, S.J.; Fernandez, C. Tungsten-molybdenum oxide nanowires/reduced graphene oxide nanocomposite with enhanced and durable performance for electrocatalytic hydrogen evolution reaction. *Int. J. Hydrog. Energy* **2017**, *42*, 8130–8138. [CrossRef]

173. Ma, L.; Shen, X.; Zhou, H.; Zhu, G.; Ji, Z.; Chen, K. CoP nanoparticles deposited on reduced graphene oxide sheets as an active electrocatalyst for the hydrogen evolution reaction. *J. Mater. Chem. A* **2015**, *3*, 5337–5343. [CrossRef]

174. Chen, R.; Song, Y.; Wang, Z.; Gao, Y.; Sheng, Y.; Shu, Z.; Zhang, J.; Li, X.A. Porous nickel disulfide/reduced graphene oxide nanohybrids with improved electrocatalytic performance for hydrogen evolution. *Catal. Commun.* **2016**, *85*, 26–29. [CrossRef]

175. Liu, H.; He, P.; Wang, S.; Gao, J.; Zhou, L.; Li, C.; Zhang, Y.; Yang, D.; He, M.; Jia, L.; et al. Facile one-step fabrication of bimetallic Co–Ni–P hollow nanospheres anchored on reduced graphene oxide as highly efficient electrocatalyst for hydrogen evolution reaction. *Int. J. Hydrog. Energy* **2019**, *44*, 24140–24150. [CrossRef]

176. Darabdhara, G.; Amin, M.A.; Mersal, G.A.; Ahmed, E.M.; Das, M.R.; Zakaria, M.B.; Malgras, V.; Alshehri, S.M.; Yamauchi, Y.; Szunerits, S.; et al. Reduced graphene oxide nanosheets decorated with Au, Pd and Au–Pd bimetallic nanoparticles as highly efficient catalysts for electrochemical hydrogen generation. *J. Mater. Chem. A* **2015**, *3*, 20254–20266. [CrossRef]

177. Ojha, K.; Sharma, M.; Kolev, H.; Ganguli, A.K. Reduced graphene oxide and MoP composite as highly efficient and durable electrocatalyst for hydrogen evolution in both acidic and alkaline media. *Catal. Sci. Technol.* **2017**, *7*, 668–676. [CrossRef]

178. Guruprasad, K.; Maiyalagan, T.; Shanmugam, S. Phosphorus doped MoS2 nanosheet promoted with nitrogen, sulfur dual doped reduced graphene oxide as an effective electrocatalyst for Hydrogen evolution reaction. *Acs Appl. Energy Mater.* **2019**, *2*, 6184–6194. [CrossRef]

179. Chen, Z.; Wu, H.; Li, J.; Wang, Y.; Guo, W.; Cao, C.; Chen, Z. Defect enhanced CoP/Reduced graphene oxide electrocatalytic hydrogen production with pt-like activity. *Appl. Catal. B Environ.* **2020**, *265*, 118576. [CrossRef]

180. Yao, T.; An, X.; Han, H.; Chen, J.Q.; Li, C. Photoelectrocatalytic materials for solar water splitting. *Adv. Energy Mater.* **2018**, *8*, 1800210. [CrossRef]

181. Etacheri, V.; Valentin, C.D.; Schneider, J.; Bahnemann, D.; Pillai, S.C. Visible-light activation of TiO2 photocatalysts: Advances in theory and experiments. *J. Photochem. Photobiol. C* **2015**, *25*, 1–29. [CrossRef]

182. Haussener, S.; Xiang, C.; Spurgeon, J.M.; Ardo, S.; Lewis, N.S.; Weber, A.Z. Modeling, simulation, and design criteria for photoelectrochemical water-splitting systems. *Energy Environ. Sci.* **2012**, *5*, 9922–9935. [CrossRef]

183. Park, H.G.; Holt, J.K. Recent advances in nanoelectrode architecture for photochemical hydrogen production. *Energy Environ. Sci.* **2010**, *3*, 1028–1036. [CrossRef]

184. Qorbani, M.; Naseri, N.; Moradlou, O.; Azimirad, R.; Moshfegh, A.Z. How CdS nanoparticles can influence TiO2 nanotube arrays in solar energy applications? *Appl. Catal. B Environ.* **2015**, *162*, 210–216. [CrossRef]

185. Walter, M.G.; Warren, E.L.; McKone, J.R.; Boettcher, S.W.; Mi, Q.; Santori, E.A.; Lewis, N.S. Solar water splitting cells. *Chem. Rev.* **2010**, *110*, 6446–6473. [CrossRef] [PubMed]

186. Li, R. Latest progress in hydrogen production from solar water splitting via photocatalysis, photoelectrochemical, and photovoltaic-photoelectrochemical solutions. *Chin. J. Catal.* **2017**, *38*, 5–12. [CrossRef]

187. Hisatomi, T.; Kubota, J.; Domen, K. Recent advances in semiconductors for photocatalytic and photoelectrochemical water splitting. *Chem. Soc. Rev.* **2014**, *43*, 7520–7535. [CrossRef]

188. Passalacqua, R.; Perathoner, S.; Centi, G. Semiconductor, molecular and hybrid systems for photoelectrochemical solar fuel production. *J. Energy Chem.* **2017**, *26*, 219–240. [CrossRef]

189. Gholipour, M.R.; Dinh, C.T.; Be'land, F.; Do, T.O. Nanocomposite heterojunctions as sunlight-driven photocatalysts for hydrogen production from water splitting. *Nanoscale* **2015**, *7*, 8187–8208. [CrossRef]

190. Moniz, S.J.A.; Shevlin, S.A.; Martin, D.J.; Guo, Z.X.; Tang, J. Visible-light driven heterojunction photocatalysts for water splitting a critical review. *Energy Environ. Sci.* **2015**, *8*, 731–759. [CrossRef]

191. Maeda, K. Photocatalytic water splitting using semiconductor particles: History and recent developments. *J. Photochem. Photobiol. C* **2011**, *12*, 237–268. [CrossRef]

192. Lianos, P. Review of recent trends in photoelectrocatalytic conversion of solar energy to electricity and hydrogen. *Appl. Catal. B: Environ.* **2017**, *210*, 235–254. [CrossRef]

193. Cho, Y.J.; Kim, H.I.; Lee, S.; Choi, W. Dual-functional photocatalysis using a ternary hybrid of TiO_2 modified with graphene oxide along with Pt and fluoride for H2-producing water treatment. *J. Catal.* **2015**, *330*, 387–395. [CrossRef]

194. Lee, D.K.; Han, K.S.; Shin, W.H.; Lee, J.W.; Choi, J.H.; Choi, K.M.; Lee, Y.; Kim, H.I.; Choi, W.; Kang, J.K. Graphitic domain layered titania nanotube arrays for separation and shuttling of solar-driven electrons. *J. Mater. Chem. A* **2013**, *1*, 203–207. [CrossRef]

195. Moon, G.H.; Kim, H.I.; Shin, Y.; Choi, W. Chemical-free growth of metal nanoparticles on graphene oxide sheets under visible light irradiation. *Rsc Adv.* **2012**, *2*, 2205–2207. [CrossRef]

196. Soltani, T.; Tayyebi, A.; Lee, B.K. Efficient promotion of charge separation with reduced graphene oxide (rGO) in BiVO4/rGO photoanode for greatly enhanced photoelectrochemical water splitting. *Sol. Energy Mater. Sol. Cells.* **2018**, *185*, 325–332. [CrossRef]

197. Ghorbani, M.; Abdizadeh, H.; Taheri, M.; Golobostanfard, M.R. Enhanced photoelectrochemical water splitting in hierarchical porous ZnO/Reduced graphene oxide nanocomposite synthesized by sol-gel method. *Int. J. Hydrog. Energy* **2018**, *43*, 7754–7763. [CrossRef]

198. Chen, D.; Zhang, H.; Liu, Y.; Li, J. Graphene and its derivatives for the development of solar cells, photoelectrochemical, and photocatalytic applications. *Energy Environ. Sci.* **2013**, *6*, 1362–1387. [CrossRef]

199. Opoku, F.; Govender, K.K.; van Sittert, C.G.C.E.; Govender, P.P. Tuning the electronic structures, work functions, optical properties and stability of bifunctional hybrid graphene oxide/V–doped $NaNbO_3$ type–II heterostructures: A promising photocatalyst for H_2 production. *Carbon* **2018**, *136*, 187–195. [CrossRef]

200. Nayak, S.; Parida, K. Recent progress in LDH@graphene and analogous heterostructures for highly active and stable photocatalytic and photoelectrochemical water splitting. *Chem. Asian J.* **2021**, *16*, 2211–2248. [CrossRef]

201. Samsudin, M.F.R.; Ullah, H.; Tahir, A.A.; Li, X.; Ng, Y.H.; Sufian, S. Superior photoelectrocatalytic performance of ternary structural BiVO4/GQD/g-C3N4 heterojunction. *J. Colloid Interface Sci.* **2021**, *586*, 785–796. [CrossRef]

202. Cheng, Q.; Xu, J.; Wang, T.; Fan, L.; Ma, R.; Yu, X.; Zhu, J.; Xu, Z.; Lu, B. Double quantum dots decorated 3D graphene flowers for highly efficient photoelectrocatalytic hydrogen production. *Appl. Surf. Sci.* **2017**, *422*, 528–535. [CrossRef]

203. Carraro, F.; Calvillo, L.; Cattelan, M.; Favaro, M.; Righetto, M.; Nappini, S.; Pis, I.; Celorrio, V.; Fermín, D.J.; Martucci, A.; et al. Fast one-pot synthesis of MoS2/crumpled graphene p–n nanonjunctions for enhanced photoelectrochemical hydrogen production. *Acs Appl. Mater. Interfaces* **2015**, *7*, 25685–25692. [CrossRef] [PubMed]

204. Garcia, A.; Albero, J.; García, H. Multilayer N-doped Graphene Films as Photoelectrodes for H2 Evolution. *ChemPhotoChem* **2017**, *1*, 388–392. [CrossRef]

205. Yuan, X.; Xu, Y.; Meng, H.; Han, Y.; Wu, J.; Xu, J.; Zhang, X. Fabrication of ternary polyaniline-graphene oxide-TiO2 hybrid films with enhanced activity for photoelectrocatalytic hydro-gen production. *Sep. Purif. Technol.* **2018**, *193*, 358–367. [CrossRef]

206. Shaban, M.; Rabia, M.; El-Sayed, A.M.A.; Ahmed, A.; Sayed, S. Photocatalytic properties of PbS/graphene oxide/polyaniline electrode for hydrogen generation. *Sci. Rep.* **2017**, *7*, 1–13. [CrossRef] [PubMed]

207. Gupta, S.; Subramanian, V. Encapsulating Bi2Ti2O7 (BTO) with reduced graphene oxide (RGO): An effective strategy to enhance photocatalytic and photoelectrocatalytic activity of BTO. *Acs Appl. Mater. Interfaces* **2014**, *6*, 18597–18608. [CrossRef] [PubMed]

208. Zhao, X.; Pan, D.; Chen, X.; Li, R.; Jiang, T.; Wang, W.; Li, G.; Leung, D.Y. g-C3N4 photoanode for photoelectrocatalytic synergistic pollutant degradation and hydrogen evolution. *Appl. Surf. Sci.* **2019**, *467*, 658–665. [CrossRef]

209. Akyüz, D.; Ayaz, R.M.Z.; Yılmaz, S.; Uğuz, O.; Sarıoğlu, C.; Karaca, F.; Özkaya, A.R.; Koca, A. Metal chalcogenide based photocatalysts decorated with heteroatom doped reduced graphene oxide for photocatalytic and photoelectrochemical hydrogen production. *Int. J. Hydrog. Energy* **2019**, *44*, 18836–18847. [CrossRef]

210. Samsudin, M.F.R.; Sufian, S. Hybrid 2D/3D g-C3N4/BiVO4 photocatalyst decorated with RGO for boosted photoelectrocatalytic hydrogen production from natural lake water and photocatalytic degradation of antibiotics. *J. Mol. Liq.* **2020**, *314*, 113530. [CrossRef]

211. Dargahi, Z.; Asgharzadeh, H.; Ghaleh, H.M. Synthesis of Mo-doped TiO2/reduced graphene oxide nanocomposite for photoelectrocatalytic applications. *Ceram. Int.* **2018**, *44*, 13015–13023. [CrossRef]

212. Rambabu, Y.; Dhua, S.; Jaiswal, M.; Roy, S.C. High photoelectrochemical performance of reduced graphene oxide wrapped, CdS functionalized, TiO2 multi-leg nanotubes. *Nanotechnology* **2020**, *31*, 275701. [CrossRef]

213. Rambabu, Y.; Jaiswal, M.; Roy, S.C. Enhanced photo-electrochemical performance of reduced graphene-oxide wrapped TiO$_2$ multi-leg nanotubes. *J. Electrochem. Soc.* **2016**, *163*, H652. [CrossRef]

214. Long, Z.; Tong, X.; Liu, C.; Channa, A.I.; Wang, R.; Li, X.; Lin, F.; Vomiero, A.; Wang, Z.M. Near-infrared, eco-friendly ZnAgInSe quantum dots-sensitized graphene oxide-TiO2 hybrid photoanode for high performance photoelectrochemical hydrogen generation. *Chem. Eng. J.* **2021**, *426*, 131298. [CrossRef]